How to Cite: Alibrahimi, A.A., & Abdul-Hassan, W.S. (2026). Design and Synthesis of Novel Molecular Switches Functionalized with a Viologen Unit Based on Copper(II) Bis(ethyl 4-chloroacetoacetate) Complex. *Eurasian Journal of Chemistry.* https://doi.org/10.31489/2959-0663/2-26-1

Article

Received: 3 November 2025 | Revised: 20 April 2026 | Accepted: 12 May 2026 | Published online: 22 May 2026

UDC 544.42+519.242.7

https://doi.org/10.31489/2959-0663/2-26-1

Ahmed A. Alibrahimi*, Wathiq S. Abdul-Hassan

Department of Chemistry, College of Science, University of Thi-Qar, Nassiria, Iraq
*(*Corresponding author's e-mail: ahmedoudah501@gmail.com)*

Design and Synthesis of Novel Molecular Switches Functionalized with a Viologen Unit Based on Copper(II) Bis(ethyl 4-chloroacetoacetate) Complex

Viologen-based molecular switches have attracted significant attention due to their reversible redox properties and promising applications in electronic and sensing devices. This study focuses on the design and development of novel chemically and electrochemically responsive molecular switches constructed through non-covalent π–dimerization of viologen radicals within copper(II) β-diketone complexes in solution. Initially, the bidentate O_2 donor ligand ethyl 4-chloroacetoacetate were coordinated to copper(II) to afford the base complexes CuECl, respectively. Subsequent axial coordination of CuECl with the neutral ligand 4,4′-bipyridine (bpy) led to the corresponding functionalized viologen system: $CuEV^{+}{\cdot}Cl^{-}$. Moreover, S_N2 nucleophilic substitution reactions of CuECl with bpy, afforded the additional complex $CuEV^{+}{\cdot}Cl^{-}$. A total of eleven complexes were successfully synthesized and comprehensively characterized using FT-IR, LC-mass spectrometry, TGA, DTA, DSC, XRD, EDS, and UV–visible absorption spectroscopy, along with electrochemical and reduction studies. Finally, chemical and electrochemical reduction of the viologen unit in, $CuEV^{+}{\cdot}Cl^{-}$ produced intra and intermolecular π-dimers of the resulting viologen radicals. Additionally, interactions of CuECl with bpy was examined in DMF solution, and the absorption spectra of these mixtures were compared with those of the corresponding adduct complexes.

Keywords: molecular switches, viologen, dimerization, copper(II) complexes, 4,4′-bipyridine, ethyl 4-chloroacetoacetate, β-diketone, bidentate ligand

Introduction

The magnetic behavior of π-radical systems is inherently governed by their aggregation state. In the paramagnetic regime, these radicals predominantly exist as discrete π-mers bearing unpaired electrons, which results in a measurable magnetic moment. In contrast, strong intermolecular interactions promote π-dimerization, leading to complete spin pairing and consequently, the loss of paramagnetism. This reversible paramagnetic–diamagnetic transition, extensively documented in viologen and tetrathiafulvalene derivatives, is a hallmark of radical π-systems and constitutes a key topic in contemporary supramolecular and materials chemistry [1, 2].

Viologens are a family of organic salts derived from 4,4′-bipyridyl with the general formula $(C_5H_4NR)_2^{n+}$. They are best known for their intensely colored blue derivatives and their facile, reversible redox behavior. Upon one-electron reduction, viologens are converted into highly colored radical monocations, typically exhibiting violet hues, and can undergo multiple reversible color changes upon successive reduction and oxidation cycles. The term "viologen" was first introduced by Michaelis in 1933 after observing the emergence of a violet coloration resulting from the one-electron reduction of 1,1′-dimethyl or 4,4′-bipyridinium salt (DMV^{2+}), leading to the generation of a radical cation dimer [3, 4].

A molecular switch is defined as a molecule capable of reversibly interconverting between at least two (or more) stable states under the influence of external stimuli such as thermal, chemical, electrical, or optical inputs. In this context, viologen radical cations display intense coloration and high molar absorptivity, attributed to intramolecular charge transfer between the +1 and neutral nitrogen centers. In aqueous media, for instance, the blue methyl viologen radical cation can shift to a purple color at higher concentrations. Upon heating, the purple solutions revert to blue, and this color change is fully reversible. Such dimerization of viologen radicals in water is widely recognized [5–7].

The present study was designed with two primary objectives. First, to synthesize and characterize the copper(II) complex of (CuECl) and its corresponding bipyridine terminal to investigate the formation of the viologen-based complex $CuEV^{+}{\cdot}Cl^{-}$, obtained by combining CuECl with a propylene-spacer viologen (V^{+}).

Second, particular attention was given to monitoring the redox-induced π-dimerization of the $CuEV^{+}\cdot Cl^{-}$ complex by chemical and electrochemical reduction.

Experimental

Instruments

FT-IR spectra of the metal complexes were recorded on KBr pellets using a SHIMADZU FT-IR Affinity analytical apparatus (Japan) over the range 150–4000 cm^{-1}. UV–Visible absorption spectra were obtained in 1 cm quartz cuvettes using a PG Instruments T90+ spectrophotometer (UK) in the wavelength range of 200–900 nm. Thermal stability of the complexes was investigated by thermogravimetric analysis (TGA) using an SDT Q600 V20.9 thermal analyzer (TA Instruments, USA). Powder X-ray diffraction (XRD) patterns were collected on a PANalytical diffractometer (Netherlands) with Cu Kα radiation (λ ≈ 1.5406 Å). Molecular ions were analyzed using an Agilent 5973 Network LC–mass spectrometer (USA) operating in electron ionization (EI) mode at 70 eV. Electrochemical properties were examined by cyclic voltammetry (CV) using a PARSTAT 4000 electrochemical workstation (Princeton Applied Research, USA) under an argon atmosphere at room temperature.

Chemical Reagents

All chemical reagents and solvents were of analytical grade and used as received without further purification. The following compounds were purchased from Energy Chemical (China): ethyl 4-chloroacetoacetate (98 %); Hyper Chem (China): 4,4'-bipyridine (98 %) and Zn powder (99.9 %); Inter-chimiques (France): methyl iodide (99.9 %); Thomas Baker (India): copper(II) acetate monohydrate (99 %) and acetone (99 %); Alpha Chemika (India): methanol (99.7 %) and dichloromethane (99.8 %); Loba Chemie (Belgium): ethanol (99.8 %), acetonitrile (99.5 %), N,N-dimethylformamide (99.8 %), and hydrochloric acid (37 %); Scharlau (Spain): ethyl acetate (99.9 %); Romil (UK): benzene (99.7 %) and hexane (99 %); and Merck (Germany): dimethyl sulfoxide (DMSO, 99 %).

Methods of Synthesis

Synthesis of CuECl Complex

A solution of ethyl 4-chloroacetoacetate (2 mL, 14.8004 mmol, 2 eq) dissolved in MeOH (1 mL) was added dropwise over 10 min with stirring to a solution of copper(II) acetate monohydrate (1.344 g, 7.4 mmol, 1 eq) dissolved in a 1:1 methanol–water mixture (10 mL). The reaction mixture was stirred for 1 h, then heated at 60 °C for 2 h. The progress of the reaction was monitored by TLC (ethyl acetate : hexane, 7:3). The resulting precipitate was collected by filtration, washed with a 1:1 H_2O–MeOH mixture, and dried under vacuum to afford CuECl as a green solid (Scheme 1). Green solid, yield: 81 % (2.3 g), M.P.: 170–172 °C, soluble in H_2O, MeOH, EtOH, MeCN, acetone, DCM, C_6H_6, EtOAc, DMF and DMSO. FT-IR (KBr disc, cm^{-1}): 2983 (aliphatic C–H), 1600, 1530 (C=C coupled with C=O and C=N), 1414, 1360, 1310 (aromatic and olefinic C–H bending), 1360, 1310 (aliphatic C–H bending), 1181, 1138 (C–O), 791, 767 (C–C stretching), 668 (C–Cl bending), 577 (Cu–O).

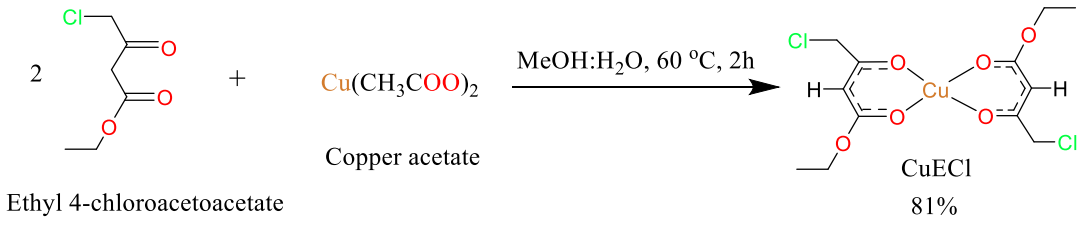

Scheme 1. Synthesis of bis(ethyl 4-chloroacetoacetate)copper(II)

Synthesis of $CuEV^{+}\cdot Cl^{-}$ Complex

A solution of bpy (0.5 g, 3.2012 mmol, 2 eq) dissolved in DMF (1 mL) was added gradually with stirring over 1 min to a hot solution of CuECl (0.6260 g, 1.600 mmol, 1 eq) dissolved in DMF (2.5 mL). The reaction mixture was heated at 60 °C for 80 min under an argon atmosphere. The progress of the reaction was monitored by TLC (MeCN : H_2O : saturated KNO_3, 10:1:1). The resulting precipitate was collected by filtration and dried under vacuum to afford $CuEV^{+}\cdot Cl^{-}$ as a grey solid (Scheme 2). Grey solid, yield: 69 %

(0.73 g), M.P.: 156–158 °C, sparingly soluble in H_2O, MeOH, EtOH, MeCN, DMF and DMSO. FT-IR (KBr disc, cm^{-1}): 3068, 3047 (aromatic C–H and C=C–H stretching), 2979, 2955, 2900 (aliphatic C–H), 1654, 1610, 1551 (C=C coupled with C=O and C=N), 1472, 1419 (aromatic and olefinic C–H bending), 1364 (aliphatic C–H bending), 1270, 1216 (C–N), 1175 (C–O), 759 (C–C stretching), 642 (C–Cl bending), 575 (Cu–O).

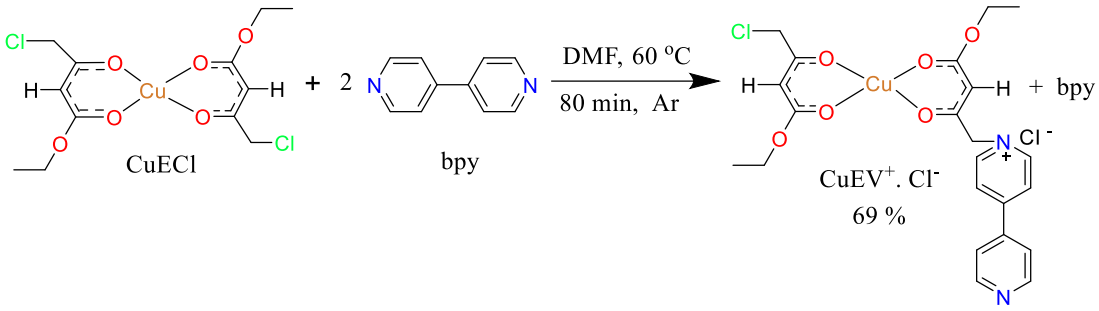

Scheme 2. Synthesis of $CuEV^{+}\cdot Cl^{-}$ complex

Results and Discussion

FTIR Spectra of Copper Complexes

FTIR spectra of the complexes CuECl and $CuEV^{+}\cdot Cl^{-}$ were recorded and are presented in Figures S1 and S2; the corresponding FT-IR spectral data are listed in Table 1.

Table 1

Important FT-IR data of Cu(II) complexes

CuECl	$CuEV^{+}\cdot Cl^{-}$	Assignment
–	3068, 3047	C–H of both stretch aromatic and C=C–H
2983	2979, 2955, 2900	Aliphatic C–H
1600, 1530	1610, 1654, 1551	C=C coupled with C=O and C=N
1414, 1360, 1310	1472, 1419	Aromatic and olefinic C–H bending
1360, 1310	1364	Aliphatic C–H bending
–	1270, 1216	C–N
1181, 1138	1175	C–O
791, 767	759	Stretching C–C
668	642	Bending C–Cl
577	575	Cu–O

Aromatic and olefinic C–H stretching vibrations are observed in the 3100–3000 cm^{-1} region. Specifically, the FT-IR spectrum of CuECl exhibits a band at 3098 cm^{-1}, while the terminally bound species $CuEV^{+}\cdot Cl^{-}$ shows a characteristic peak at 3068 cm^{-1}. These features are diagnostic of the retention of the aromatic and olefinic C–H environments upon coordination [8].

Aliphatic C–H stretching is observed in <3000 cm^{-1} region. Bands at 2983 cm^{-1} for CuECl correspond to ν(C–H) of aliphatic methylene groups. Terminal species give bands at 2979, 2955 and 2900 cm^{-1} ($CuEV^{+}\cdot Cl^{-}$), these confirm the presence of alkyl substituents on the viologen or bipyridine units [9].

C=O and C=C stretching of the β-diketonate core is observed in the 1710 and 1500 cm^{-1} regions. The base complexes show characteristic β-diketonate bands at 1600 and 1530 cm^{-1} (CuECl). Terminally bound species show 1654, 1610 and 1551 cm^{-1} ($CuEV^{+}\cdot Cl^{-}$). These absorptions are attributed to the overlapping ν(C=O) and ν(C=C) stretches of the β-diketone backbone conjugated with coordinated nitrogen donors [10].

Aromatic and olefinic C–H bending is observed in the 1500–1300 cm^{-1} region. Bends at 1414 cm^{-1} (CuECl), terminal species exhibit 1472–1419 cm^{-1} ($CuEV^{+}\cdot Cl^{-}$). These bands confirm the retention of the aromatic character in the coordinated ligands [11].

New bands observed at 1270 and 1216 cm^{-1} for $CuEV^{+}\cdot Cl^{-}$, which are absent in the precursor and CuECl spectra, are assigned to C–N stretching vibrations. The emergence of these bands confirms the for-

mation of a new complex characterized by the expected adduct structure and terminal linkage [10]. Bending vibrations were observed at 1181, 1138 cm^{-1} for CuECl, while the terminal linkage compounds with viologen appear bands at 1175, 1090 and 1050 cm^{-1} for $CuEV^{+}\cdot Cl^{-}$, these bands are assigned to vibrational modes involving bending coupled with stretching within the C–O group [10].

The bands observed at approximately 650 and 430 cm^{-1} are assigned to C–Cl stretching and metal–ligand vibrations, respectively. Characteristic bands were identified at 668 cm^{-1} (CuECl), 642 cm^{-1} ($CuEV^{+}\cdot Cl^{-}$), and 674 and 656 cm^{-1} ($CuEC_1V_2^{2+}\cdot Cl^{-}\cdot I^{-}$). Lower-frequency peaks at 577 cm^{-1} (CuECl) is assigned to ν(Cu–O). These confirm direct coordination of both β-diketonate oxygen and bipyridine/viologen nitrogen donors to the copper(II) center [8, 9].

LC-Mass Spectrometry of Cu(II) Complexes

The LC-mass spectra of CuECl and $CuEV^{+}\cdot Cl^{-}$ are depicted in Figures S3 and S4. The LC-mass spectrum of CuECl complex exhibited a molecular ion peak at *m/z* = 391.1. Other important peaks occurred at *m/z* = 617.83 due to the dimer losing one ligand unit [2M-L]. Isotope peaks of the molecular ions due to ^{37}Cl, $[2M\text{-}L^{+}]$ and $[M^{+}Cu^{+1}]^{+}$ confirm the presence of chlorine atoms. Other importent peaks are shown in the suggested mechanism at *m/z* = 291.1, 263.1, 217, 181.91, 148.9, 115.15, 90.9 and 69 due to $[M^{\bullet+}\text{-}C_{11}H_{16}CuO_5^{+}]$, $[C_9H_{12}CuO_5^{+}]$, $[M^{\bullet+}\text{-}C_8H_{10}CuO_3^{+}]$, $[M^{\bullet+}\text{-}C_4H_4ClCuO_2^{+}]$, $[M^{\bullet+}\text{-}C_4H_5CuO_2^{+}]$, $[M^{\bullet+}\text{-}C_6H_{11}O_2^{+}]$, $[M^{\bullet+}\text{-}C_4H_7Cl^{+}]$ and $[M^{\bullet+}\text{-}C_4H_5O^{+}]$ respectively. The intensive peak (base peak) at *m/z* = 617.83, 682.49 and 709.26 are attributed $[C_{18}H_{24}Cl_3Cu_2O_9^{+}]$, $[C_{23}H_{32}Cl_2Cu_2O_{11}^{+}]$ and $[C_{19}H_{20}Cl_4Cu_2O_{12}^{+}]$ respectively [12–14].

The LC-mass spectrum of $CuEV^{+}\cdot Cl^{-}$ is depicted in Figure S4. The LC-mass spectrum of $CuEV^{+}\cdot Cl^{-}$ complex showed a peak at *m/z* = 665.38 corresponds to molecular ion $[M]^{+}$. The peak at *m/z* = 1019.84 is attributed to loss of 2 chlorine atoms and 3H from the dimer of the molecular ion $[2M\text{-}2Cl\text{-}3H]^{+}$. The peak of *m/z* = 156.95 confirm the removal of the bpy from the $CuEV^{+}\cdot Cl^{-}$ complex. Other important peaks are note at *m/z* = 464.3, 352, 311.15, 283.15, 270.20, 197.95, 270.20, 311.15, 318, 393,407.97, 462.96, 476.99, 556.53, 561, 726.16, 806.83 and 902.59 [12–14].

X-Ray Diffraction of Copper Complexes

The Powder X-ray diffraction (XRD) patterns of the Cu(II) complexes are presented in Figures S5 and S6, with the corresponding diffraction data summarized in Tables 2 and 3. The average crystallite sizes were calculated using the Scherrer-Debye equation (Eq. 1), based on the full width at half maximum (FWHM) of the high-intensity diffraction peaks:

$$D = \frac{K\lambda}{\beta}\cdot\frac{1}{\cos\theta}, \tag{1}$$

where *D* — is the average crystal size, K — is the Scheerer's constant (the shape factor with a typical value of 0.94), λ – is the wavelength of the X-ray source (0.15405 nm, 1.5405 Å for Cu Kα radiation), β — is the full width at the half maximum (FWHM) of the diffraction peak in radians, θ — is the Bragg diffraction angle [15–17].

The calculation of avenge crystallite size using the Scherrer model involves calculating the crystallite sizes (*D*) for individual peaks and then computing their mean values. Table 2 contain the mean crystallite dimensions calculated using the Scherrer equation [18].

Table 2

Average crystallite size (*D*) values of the synthesized complexes calculated using the Scherrer equation

Average crystal size, nm	
CuECl	$CuEV^{+}\cdot Cl^{-}$
34.29781605	21.89748354

Although the Scherrer equation provides a straightforward method by considering solely the contribution of physical broadening and neglecting instrumental effects, the Williamson–Hall model overcomes this limitation by simultaneously incorporating both crystallite size and lattice strain contributions. Thus, this model provides a more comprehensive analysis of peak broadening [19]:

$$\beta = \beta_1 + \beta_2, \tag{2}$$

where β — is the total broadening, β_1 — is the broadening due to the full width at half maximum FWHM of crystallite size (Scherrer equation), β_2 —is the broadening due to strain.

$$\varepsilon = \frac{\beta}{4\tan\theta} = \frac{\beta_2 \cos\theta}{4\sin\theta}. \quad (3)$$

Substituting equations 2 and 3, yields equation 4:

$$\beta = \beta_1 + \beta_2 = \frac{K\lambda}{D\cos\theta} + 4\varepsilon\frac{\sin\theta}{\cos\theta}. \quad (4)$$

After arranging the Equation 4, yields equation 5:

$$\beta\cos\theta = K\lambda/D + 4\varepsilon\sin\theta. \quad (5)$$

According to Equation (5), a plot of β cos θ (Y-axis) versus 4 sin θ (X-axis) yields a linear relationship. In this plot, the slope corresponds to the micro strain (ε), while the intercept represents Kλ/*D*, where K is the shape factor, λ is the X-ray wavelength, and *D* is the crystallite size [20, 21].

The resulting linear plots are illustrated in Figures 1 and 2.

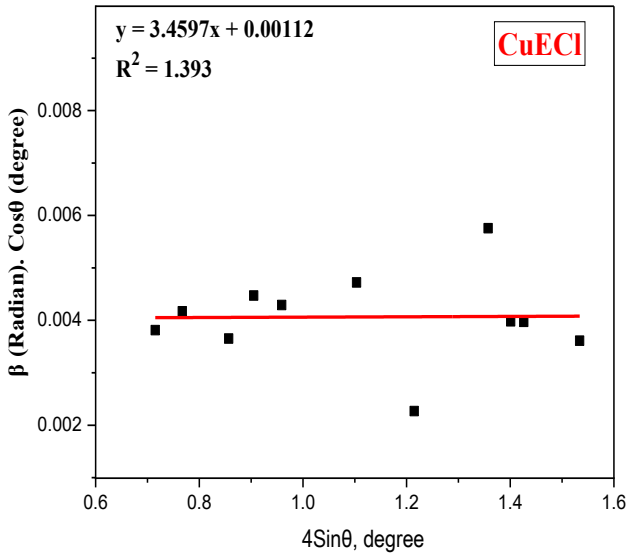

Figure 1. UDM plot of CuECl complex

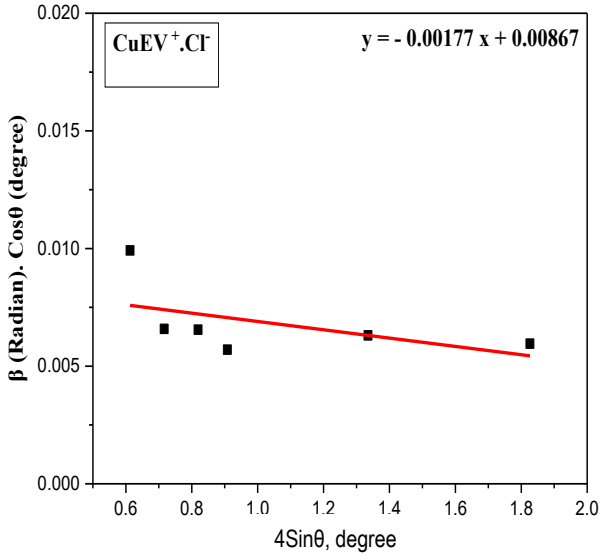

Figure 2 UDM plot of $CuEV^{+}\cdot Cl^{-}$ complex

The variations in the number and intensity of diffraction peaks, as well as the calculated crystallite sizes (*D*), provide clear evidence for the successful formation of CuECl and $CuEV^{+}\cdot Cl^{-}$ from their respective precursors. These observations also confirm the synthesis of additional copper complexes derived from CuECl. The X-ray diffraction patterns were recorded over the 10°–80° 2θ range, with the most prominent reflections appearing at 24.741° and 24.791° for CuECl, and at 23.543° for $CuEV^{+}\cdot Cl^{-}$. It is noted the complex incorporating viologen-functionalized ligand: $CuEV^{+}\cdot Cl^{-}$ keep middle crystallinity among the last three complexes and the other rest complexes .The complex CuECl showed the highest *d*-spacing.

List the *d*-spacing values both obtained from Scherrer model with those obtained frown Williamson-Hall model besides the lattice, strain values. In fact, dramatic differences are noted in both *d*-spacing and lattice strain values. As mentioned before, Scherrer model estimates *d*-spacing considering only crystallite size. But, Williamson-Hall model considers both size and lattice strain. In other words, the Scherrer model considers peak broadening that is due to crystallite size only. This model assumes the material is strain free and gives crystallite size but not strain or d-spacing changes due to strain. While, Williamson-Hall method separates peak broadening into two sources: crystallite size and lattice strain (Ɛ). Now, let us consider *d*-spacing values obtained from both models.

Firstly, the complex CuECl and showed *d*-spacing values obtained from W-H model higher than those obtained from Scherrer model. This trend indicates positive lattice strain which stretches the lattice planes of these complexes. There are distortion for the lattice and this induces tensile strain. This tensile strain causes

peak shifting to lower angles which results in increased *d*-spacing (via Bragg's law = $n\lambda = 2d \sin\theta$). Here, because W-H model account for this referred strain which shows expanded lattice planes (higher *d*). While, Scherrer und estimates the spacing since it ignores strain then lower *d*-spacing are obtained by Scherrer model [18, 19].

Table 3

Average crystallite size (*D*) values of the synthesized complexes calculated using the Williamson-Hall model

CuECl		$CuEV^{+}\cdot Cl^{-}$	
Slope = strain, ε	Crystal size *D* = Kλ/Intercept	Slope = strain, ε	Crystal size *D* = Kλ/Intercept
3.4597	58.8906774	–0.00177	16.70207612

Secondly, the complexes and $CuEV^{+}\cdot Cl^{-}$ showed W-H *d*-spacing values lower than those obtained by Scherrer model. This trend indicates that these complexes have compressive strain. This compressive strain squeezes the lattice of these complexes and reduces *d*-spacing where the peak shift to higher 2θ angles. W-H model includes this contraction in its calculation, hence lower d-spacing is noted than Scherrer *d*-spacing.

The variation in *d*-spacing between W-H and Scherrer across the prepared copper complexes reflects differences in internal strain which depend on: Ligand type (ECl, bpy, or ECl functionalized by the last three ligands). Also, this strain depends on crystal packing, symmetry, solvent inclusion or loss, defects, dislocations or coordination geometry. The expanded lattice due to tensile strain in the complex CuECl (observation of *d* (W-H) > *d* (Scherrer)) compared to the lattice contracted due to compressive strain (observation of *d* (W-H) < *d* (Sherrer)) is attributed to the presence of chloride substitution in CuECl. The chloride atom induce disorder or packing issues which increases the strain. The two Cl groups introduce larger atomic radii and distortions, causing expansion [20, 21].

The $CuEV^{+}\cdot Cl^{-}$ complex (compared to its precursor (CuECl) has compressive strain as it is clear from its negative lattice strain and W-H. *d*-spacing < Sherrer *d*-spacing. The reason of this opposite trend compared to its precursor might be the absence of Cl group which in hances the electrostatic interactions thus reducing *d*-spacing value [20, 21].

The above discussion of XRD patterns, both W-H *d*-spacing and Scheller *d*-spacing values and lattice strain values confirms the formation and the structures of the complexe CuECl. Also, it supports undoubtedly the axial coordination of the bpy and positive ligands and formation the adduct complexes. Additionally, the complexes having their ligands functionalized by viologen showed structural differences compared with either its precursor CuECl or the other adduct complexes.

Thermogravimetric Analyses of Copper Complexes

The thermal behavior of complexes CuECl and $CuEV^{+}\cdot Cl^{-}$ was investigated by thermogravimetric analysis (TGA), differential thermal analysis (DTA), and differential scanning calorimetry (DSC) up to 800 °C. The measurements were conducted at a heating rate of 10 °C/min under an argon atmosphere [22]. The TGA, DTA, and DSC curves are shown in Figures 3–7.

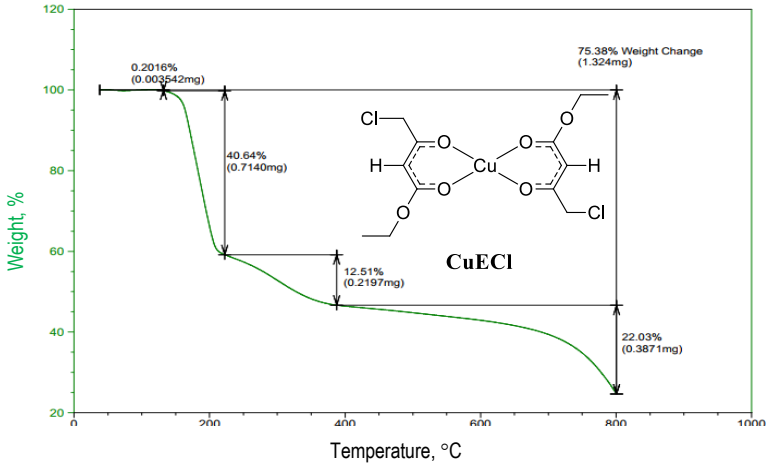

Figure 3. TGA curve of CuECl complex

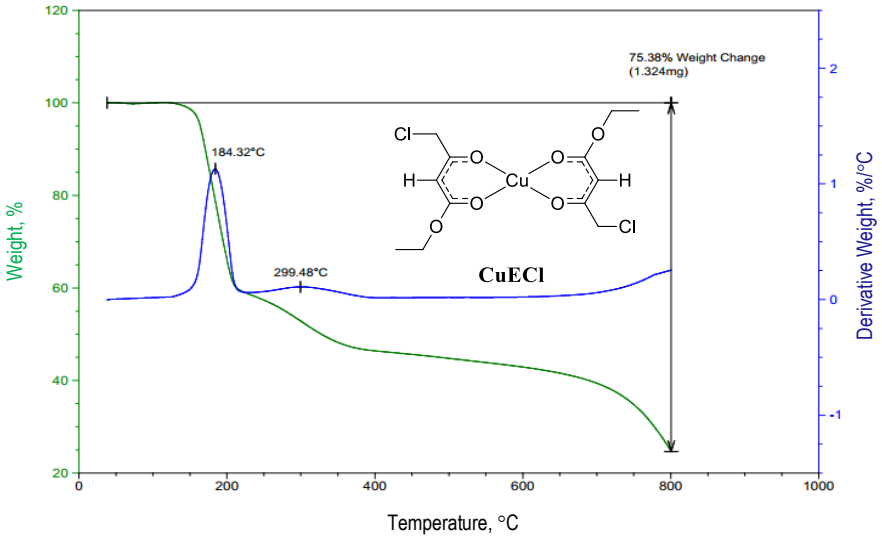

Figure 4. TGA/DTG curve of CuECl complex

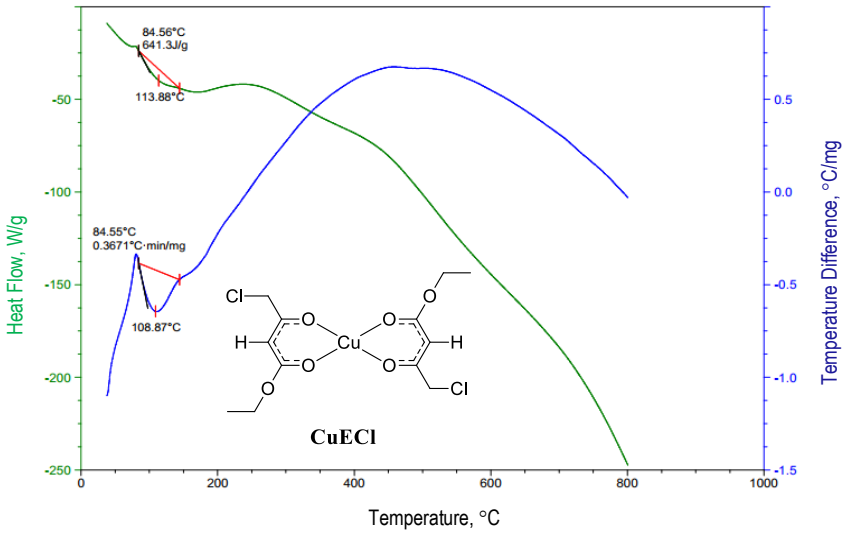

Figure 5. DSC / TGA curves of CuECl complex

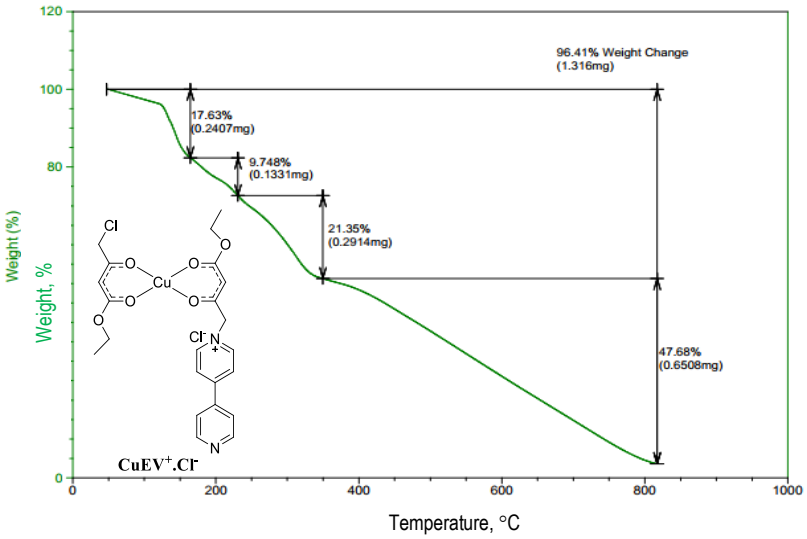

Figure 6. TGA curve of $CuEV^{+}{\cdot}Cl^{-}$ complex

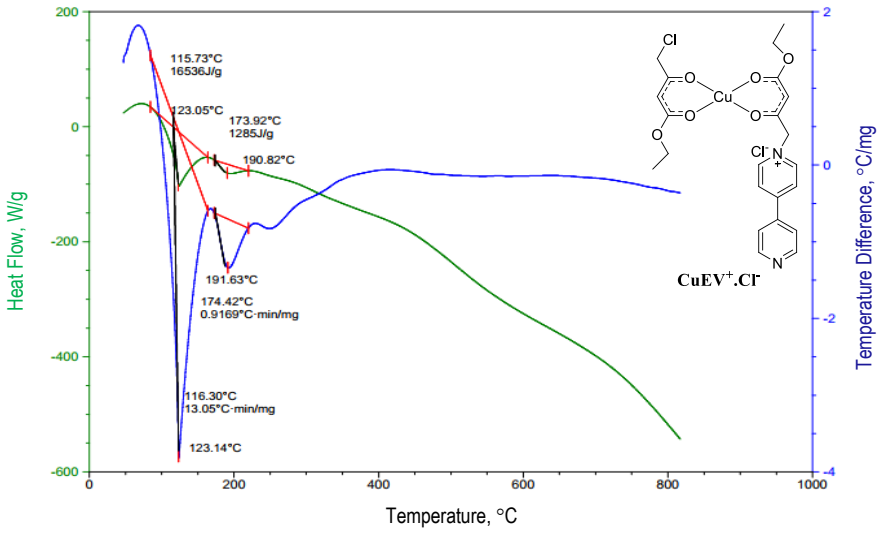

Figure 7. DSC / TGA curve of $CuEV^{+}\cdot Cl^{-}$ complex

The thermal decomposition patterns occur in four steps (for CuECl, and $CuEV^{+}\cdot Cl^{-}$). The kinetic (K_1, $t_{1/2}$ and E_a) and thermodynamic parameters (ΔH, ΔS and ΔG) of each decomposition phase are calculated for copper complexes as explained in the next item [23–26].

Calculation of Kinetic and Thermodynamic Functions of Decomposition Reaction

All thermal decomposition stages were assumed to follow first-order kinetics for the calculation of kinetic parameters. The rate constant for each decomposition stage was determined using the first-order kinetic equation:

$$\frac{dx}{dt} = k_1 \cdot (1 - x)\,, \tag{6}$$

where

$$x = \frac{w_i - w_t}{w_i - w_f}\,, \tag{7}$$

w_i — is the initial weight of each TG phase, w_t — is a weight of sample at particular time during TG phase, w_f — is the final weight at the end of TG phase, t — is the time.

Equation 8 can be written as:

$$\ln(1 - x) = -k_1 t\,. \tag{8}$$

Plotting of ln(1–x) (as y-axis) against time (min) (as x-axis) give liner relationship which confirm that TG phase are first order reaction. Slope of each line gives the value ofthe first order rate constant (k) for particular phase, see Figures 8 and 9. Half-life time ($t_{1/2}$) is determined using Equation 9:

$$t_{1/2} = \frac{0.693}{K_1}\,. \tag{9}$$

Values of k and $t_{1/2}$ are given in Tables 4 and 5 [27].

Table 4

Kinetic and thermodynamic parameters for the thermal decomposition stages of CuECl

Phase	Temperature, K	K, min^{-1}	$t_{1/2}$, min	E_a, J/mole	ΔH, J/mole	ΔS, J/mole·K	ΔG, J/mole
1	437.77	0.0047	147.44	222226.5	218586.8	–97666.74	120920
2	497.79	0.25198	2.75	94205.43	90066.65	–45141.9	135208.5
3	700.46	0.05468	12.67	7799.395	1975.56	–209924	211899.8
4	1073.74	0.02884	24.029	4800.012	4127.38	–342892	338764.4

Table 5

Kinetic and thermodynamic parameters for the thermal decomposition stages of $CuEV^{+}\cdot Cl^{-}$

Phase	Temperature, K	K, min^{-1}	$t_{1/2}$, min	E_a, J/mole	ΔH, J/mole	ΔS, J/mole. K	ΔG, J/mole
1	440.07	0.0771	8.988	29876.19	26217.34	–105925	132142.37
2	507.27	0.0355	19.52	13102.26	8884.694	–144096	152980.73
3	628.08	0.0685	10.12	17715.61	12493.6	–174537	187030.31
4	1090.32	0.0848	8.17	22618.72	13553.5	–310750	324303.28

The kinetic parameters were evaluated by applying a modified version of the Coats–Redfern method, as expressed in Equation (10):

$$\ln\left[-\ln(1-x)\right] = \ln\frac{ART^2}{\beta E_a} - \frac{E_a}{RT}, \tag{10}$$

where A — is the pre-exponential factor, β — is the heating rate (20 °C min^{-1}), R — is the universal gas constant (8.3143 J mol^{-1} K^{-1}), E_a — is the activation energy, T — is the absolute temperature expressed in Kelvin.

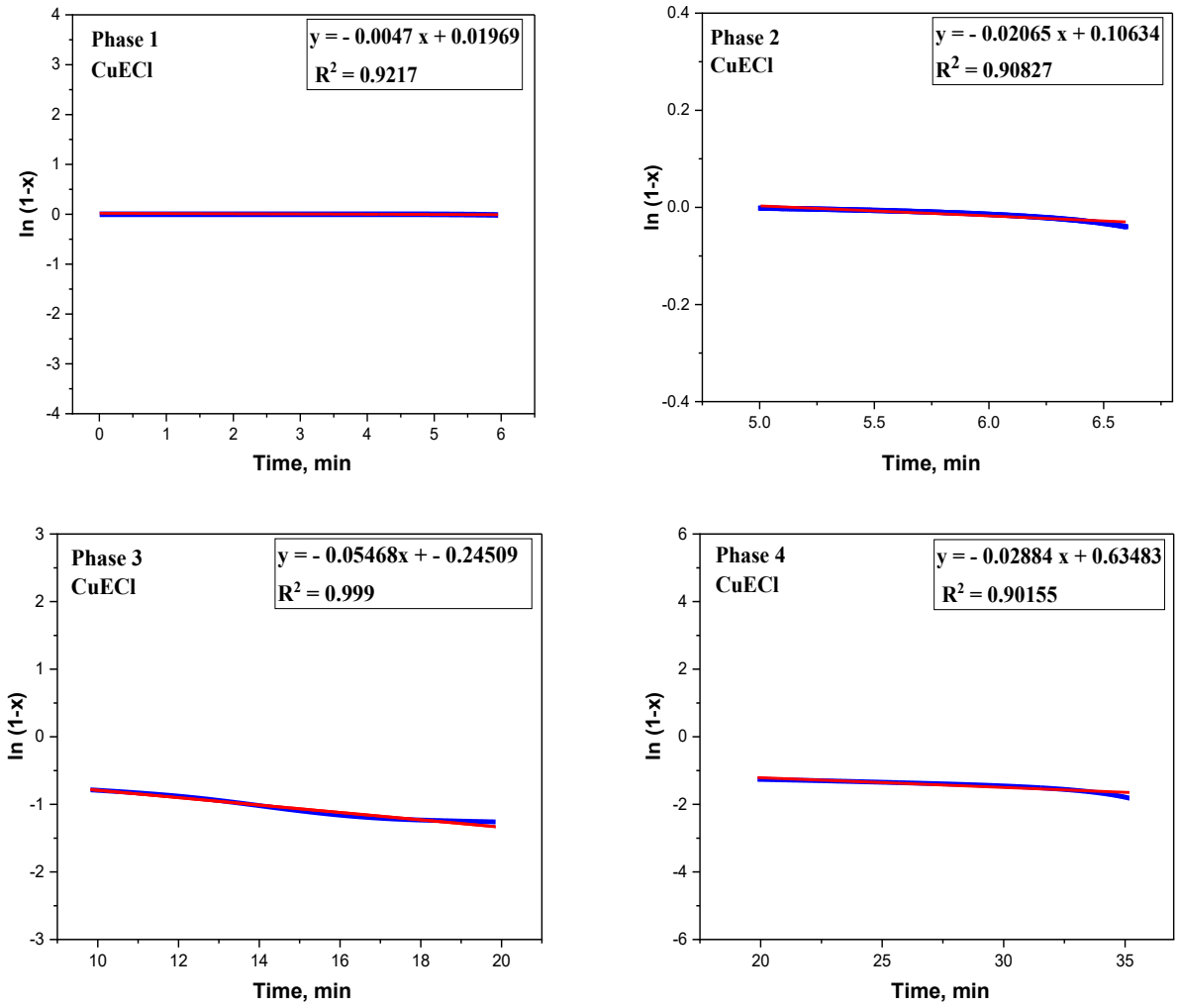

Figure 8. Plots of ln(1–x) versus time for the four decomposition stages of the CuECl complex

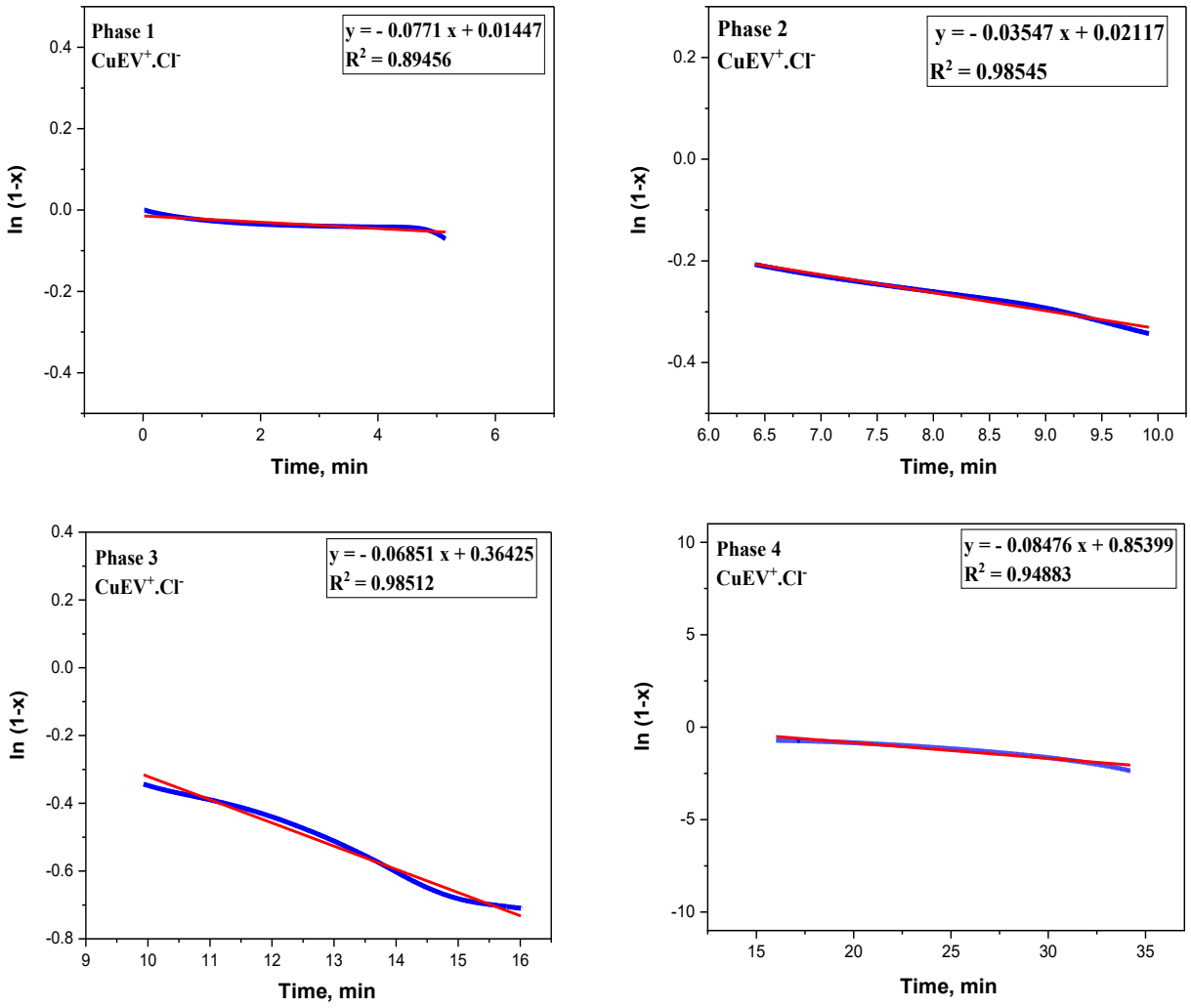

Figure 9. Plots of ln(1–x) versus time for the four decomposition stages of the $CuEV^{+}\cdot Cl^{-}$ complex

By plotting ln[–ln(1–x)] as y-axis versus 1000/T as x-axis for each phase Figures 10 and 11, linear relationship was obtained. The activation energy (E_a) and the pre-exponential factor (A) were calculated from the slope and intercept of the linear plots, respectively, according to the following equations [27]:

$$E_a = |\text{slope}| * R$$

$$A = \beta \cdot E_a \cdot \exp\frac{\text{intercept}}{RT^2}.$$

The thermodynamic parameters, including enthalpy (ΔH^*), entropy (ΔS^*), and Gibbs free energy (ΔG^*), were calculated using the following equations:

$$\Delta H^* = E_a - RT;$$

$$\Delta S^* = R\ln\left(\frac{Ah}{KT}\right);$$

$$\Delta G^* = \Delta H - T\Delta S,$$

where K — is the Boltzmann constant.

The calculated values for E_a, ΔS^*, ΔH^* and ΔG^* are summarized in Tables 4–5 [27].

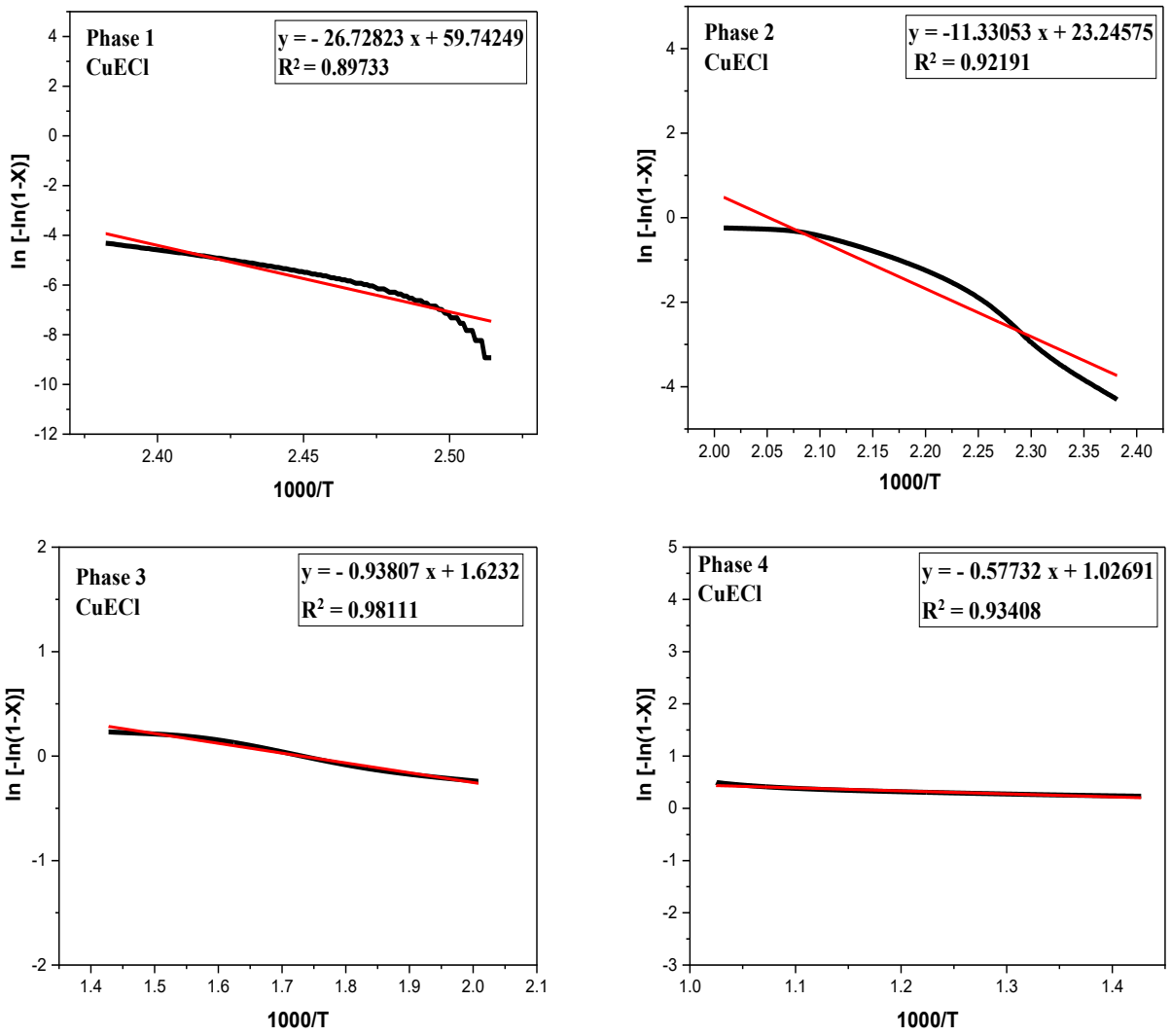

Figure 10. Plots of ln[–ln(1–x)] versus 1000/T for the four decomposition stages of the CuECl complex

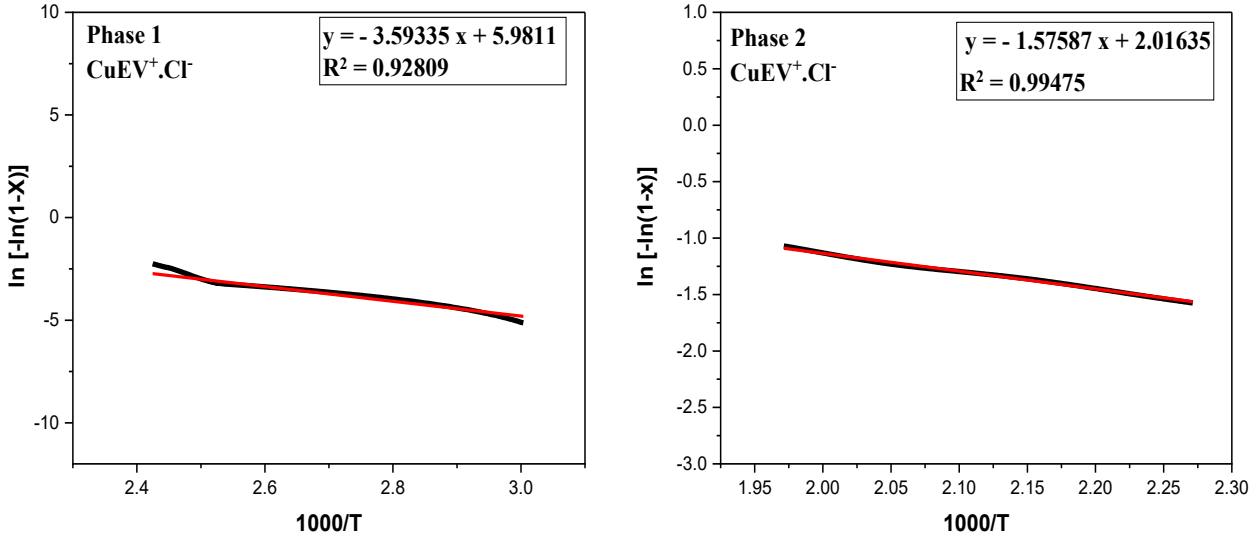

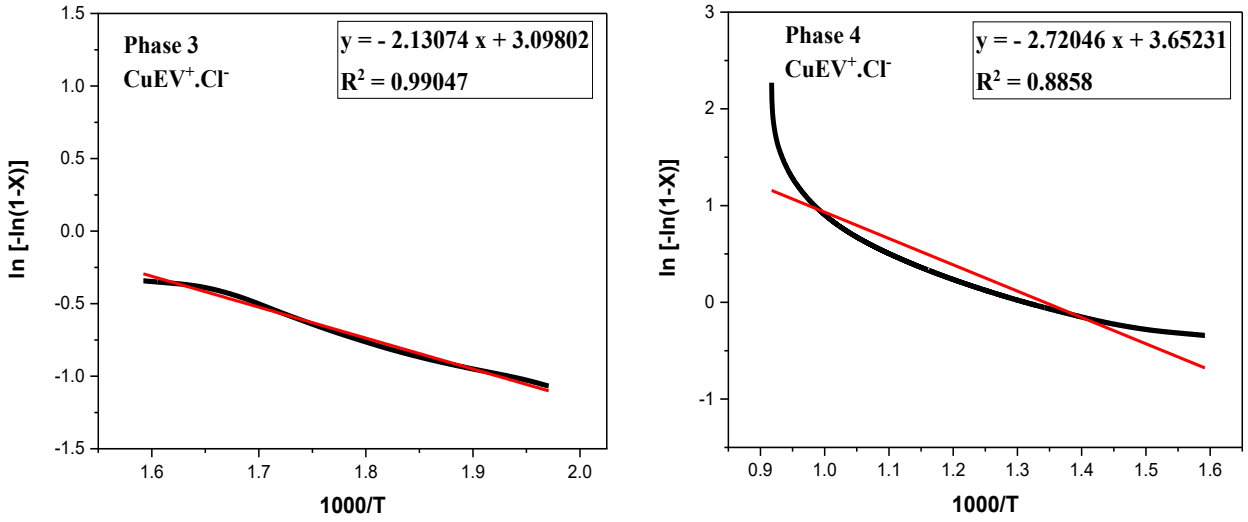

Figure 11. Plots of ln[–ln(1–x)] versus 1000/T for the four decomposition stages of the $CuEV^{+}\cdot Cl^{-}$ complex

According to the guidelines of the International Confederation for Thermal Analysis and Calorimetry (ICTAC), an increase in activation energy (E_a) among a set of compounds reflects an enhancement in their thermal stability, whereas lower E_a values correspond to reduced stability. Consequently, based on the calculated E_a values ($\times 10^3$ J·mol^{-1}) presented in Tables 4 and 5, the thermal stability of the compounds follows the sequence: $CuEV^{+}\cdot Cl^{-}$ (83312.78) < CuECl (329031.337). For the complex of the ligand functionalized with viologen, their thermal stabilities increases in the sequence: $CuEV^{+}\cdot Cl^{-}$. The thermal stability of CuECl is nearly 2.6 times higher. The thermodynamic analysis for each decomposition stage indicates that all processes are non-spontaneous and endothermic, accompanied by increases in disorder, as reflected by the negative ΔS values [23–26].

Energy Dispersive X-Ray Spectroscopy of Copper (II) Complexes (EDX)

Energy-dispersive X-ray (EDX) spectra for the copper(II) complexes are presented in Figures 12 and 13, with the corresponding scanning electron microscopy (SEM) images shown in Figures 14 and 15.

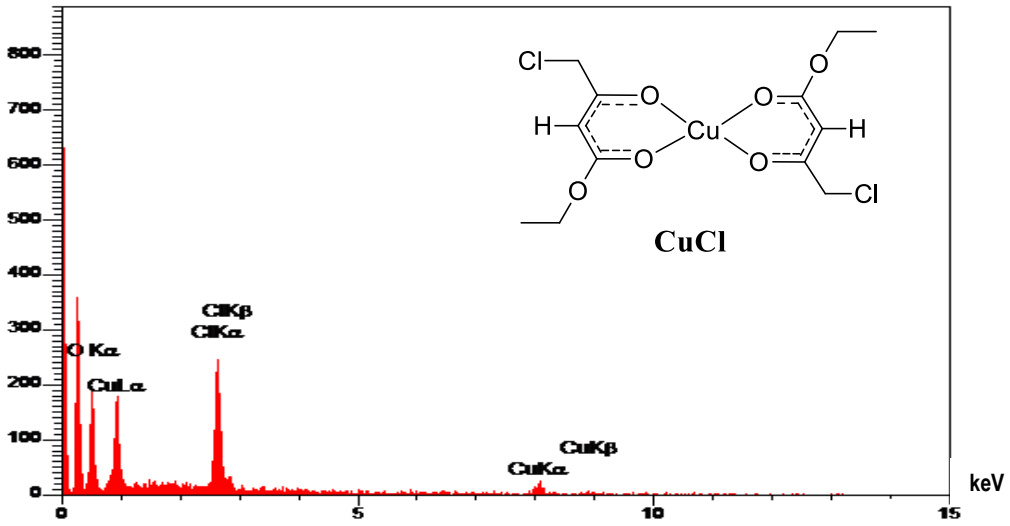

Figure 12. Energy-Dispersive X-ray (EDX) spectrum of the CuECl complex

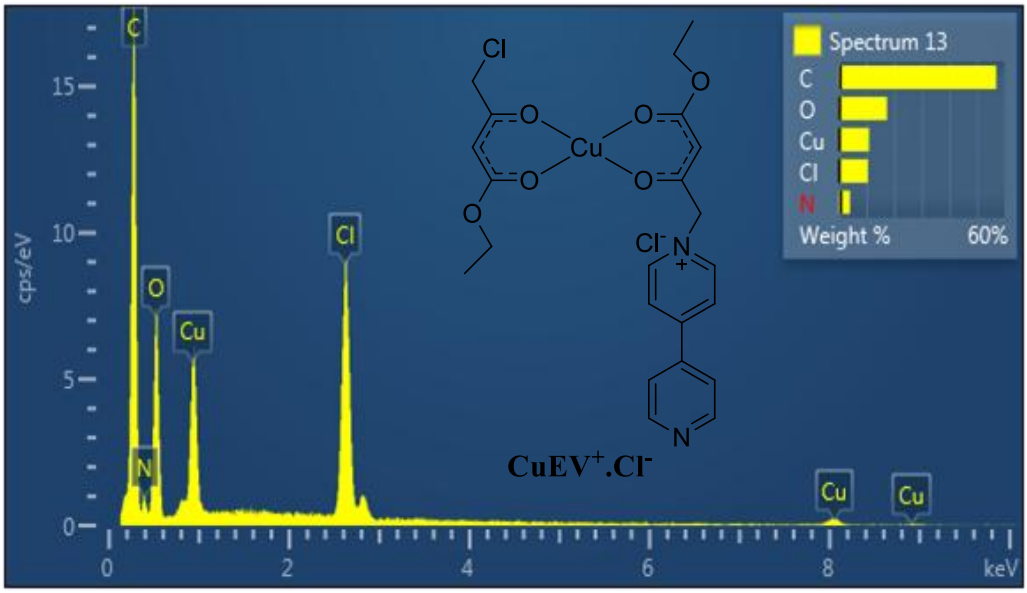

Figure 13. Energy-Dispersive X-ray (EDX) spectrum of the $CuEV^{+}\cdot Cl^{-}$ complex

The expected elements (C, O, N, Cu, I, Cl, F, Br and P) peaks are noted in the EDS spectra, which confirms and agrees with their presence in the prepared complexes. The elemental percentages that appeared in the quantitative results of this spectroscopy did not fully agree with the theoretical values of the prepared complexes. It was strangely noted that the EDS Cu% agrees only with the theoretical Cu% of CuE, and both EDS Cu% and O% showed agreement with those the theoretical of $CuEV^{+}\cdot Cl^{-}$, while other elements did not agreed in same those complexes. Undoubtedly, if one EDS or C, H, N, S and O analysis of a certain compound then the other EDS or C, H, N, S and O elements % should be agreed too. Otherwise, we should expect technical errors in the quantitative analysis of some or all the elements. Additionally, the received quantitative results of the standards are empty. For these two reasons, the quantitative results obtained from this spectroscopy should be excluded and only the qualitative results should be considered. Au and other signals observed in the EDS spectra are attributed to the coating (e.g., gold coating) and not to the sample itself [28].

Hydrogen is absent because EDS analysis can't detect it. Dramatic and typical differences are note in the SEM images among the Copper (II) complexes are depicted in Figures 20 and 21 respectively. The complex CuECl have shorter, thicker and more irregular in length and width crystals. Some CuECl crystals are stacked or clustered which indicates interrupted or altered growth. While, CuECI crystals appear rougher and more granular and this likely due to Cl substitution that disrupt regular packing as concluded before from XRD spectroscopy. The size of CuECI are shorter and broader suggesting lower crystallinity or altered nucleation rate. In term of distribution, the CuE is more aligned and compact showing better organization, while CuECl is more. Scattered oriented with possible agglomeration. Therefore, the Chlorine substitution in CuECl effects on crystal growth making it as shorter and thicker crystals. The morphology of CuECl is less regular and it has rougher surfaces. CuECl packing is less ordered. All this reflects how small ligand change, like the halogenation by chlorine can significantly Impact solid-state material properties like solubility electronic behavior. In addition to Chlorine substitution as result for mentioned difference above, the solvent effect or reaction conditions (eg., fast precipitation, low temperature) [29, 30].

A detailed comparison of the surface morphologies for the CuECl and $CuEV^{+}\cdot Cl^{-}$ complexes, as observed in the SEM images (Figures 14 and 15), is provided below. The CuECl complex displays well-defined, elongated rod- or needle-like crystals indicating high crystallinity and uniform growth along preferred directions. This is likely due to strong packing of small symmetric ligands. In contrast, $CuEV^{+}\cdot Cl^{-}$ shows irregular, blocky and aggregated particles with less-defined edges. This reflects disruption of crystal packing due to the bulkier viologen moiety. The CuECl crystals appear smooth and clean suggesting an orderly homogenous surface, the surface of an $CuEV^{+}\cdot Cl^{-}$ is rougher and more porous, possibly due to incorporation of viologen into the ligand that disrupting tight molecular packing. The crystals of CuECl are long and thin (often exceeding 10–20 μm) with relatively narrow widths. While, the $CuEV^{+}\cdot Cl^{-}$ particles are shorter and thicker with less uniform size distribution. Some particles form small fragments and others form large agglomerates. In term of distribution CuECl has highly ordered and dispersed arrangements with min-

imal aggregation. Therefore, the transition from CuECl to $CuEV^{+}\cdot Cl^{-}$ results in: loss of needle-like crystal morphology, more irregular and less crystalline texture, increased surface roughness and size heterogeneity and aggregation. These differences show how introducing bulky or charged group like viologen significantly alters the molecular self-assembly and morphology at the microstructural level. The following discussion deals with a comparison between the SEM image of $CuEV^{+}\cdot Cl^{-}$. $CuEV^{+}\cdot Cl^{-}$ has irregular and blocky particles. The structure appears disordered and amorphous compared to well-crystallized materials. In term of surface texture, $CuEV^{+}\cdot Cl^{-}$ is rough and porous.

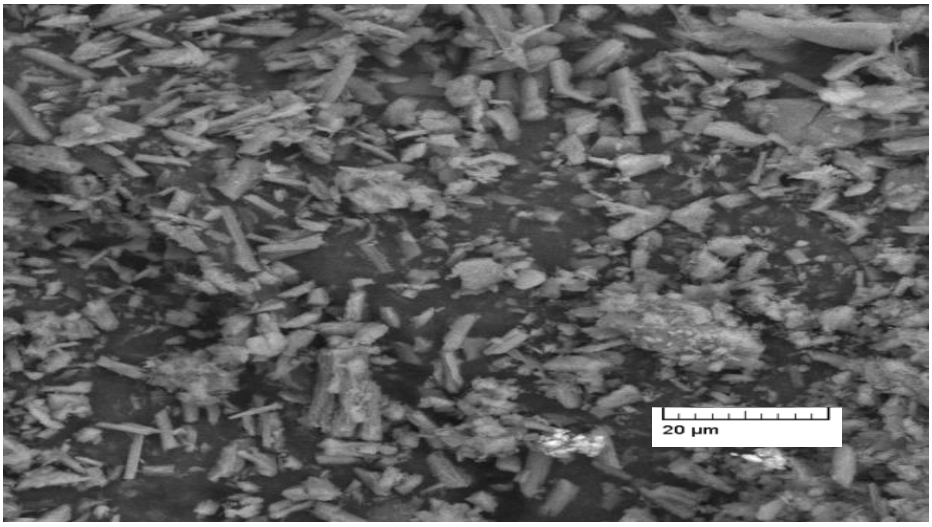

Figure 14. SEM image of CuECl complex

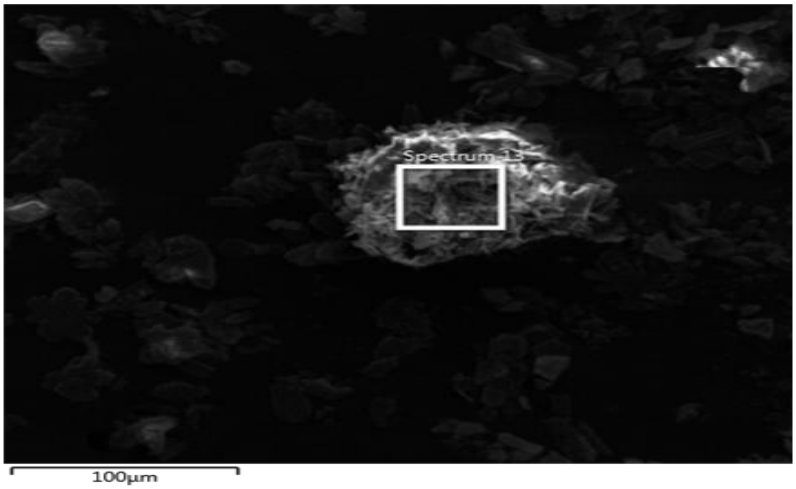

Figure 15 SEM image of $CuEV^{+}\cdot Cl^{-}$ complex

The $CuEV^{+}\cdot Cl^{-}$ has brand particle size distribution. Some particles are large aggregates and some are fine particles. The $CuEV^{+}\cdot Cl^{-}$ particles are unevenly dispersed with some regions of clustering [29, 30].

UV–Vis Characterization of Cu(II) Coordination Compounds

Show electronic absorption spectrum of CuE**C**l in different solvents are C_6H_6, EtOAc, DCM, acetone, EtOH, MeOH, ACN, DMF, DMSO and D.W with three concentrations representative in Figures 16–26 with Absorbance & wavelength (nm) along with that of copper (II) acetate two solvent ethanol and DMF.

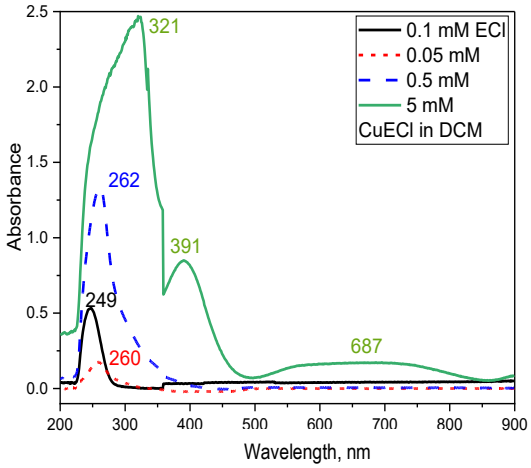

Figure 16. UV-Vis absorption spectra of ethyl acetoacetate (0.1 mM, black), copper acetate (5 mM, purple), CuECl (0.05 mM, red, (0.5 mM, blue and 5 mM, green) in EtOH

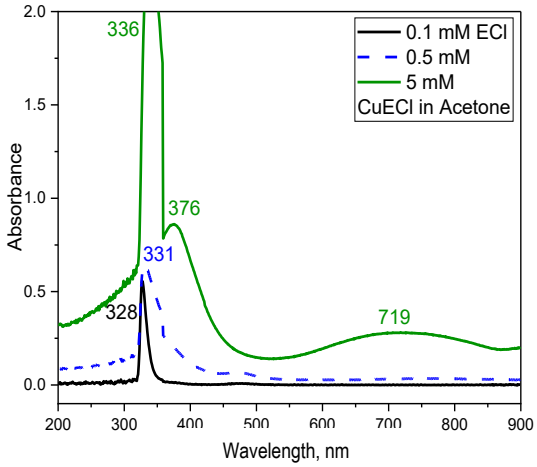

Figure 17. UV-Vis absorption spectra of ethyl 4-chloroacetoacetate (0.1 mM, black), copper acetate (5 mM, purple), CuECl (0.05 mM, red, 0.5 mM, blue and 5 mM, green) in DMF

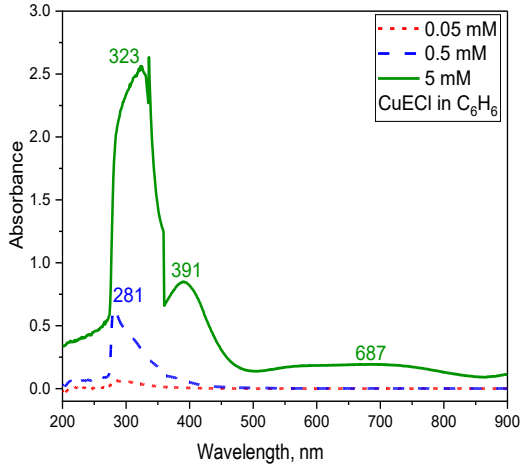

Figure 18. UV-Vis absorption spectra of CuECl (0.05 mM, red, 0.5 mM, blue and 5 mM, green) in C_6H_6

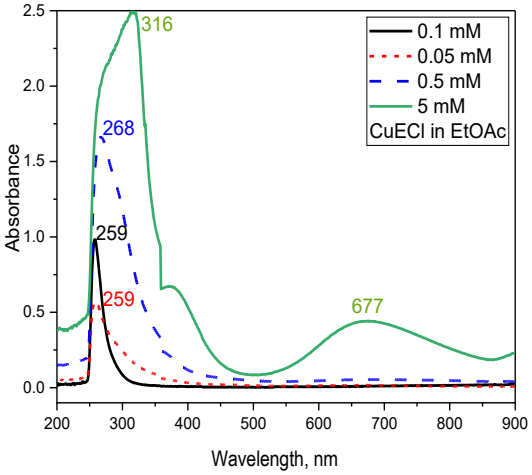

Figure 19. UV-Vis absorption spectra of ethyl 4-chloroacetoacetat (0.1 mM, black), CuECl (0.05 mM, red, 0.5 mM, blue and 0.05 mM, green) in EtOAc

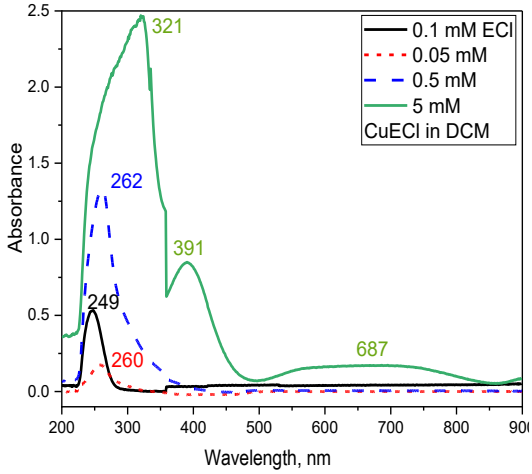

Figure 20. UV-Vis absorption spectra of ethyl 4-chloroacetoacetat (0.1 mM, black), CuECl (0.05 mM, red, 0.5 mM, blue and 5 mM, green) in DCM

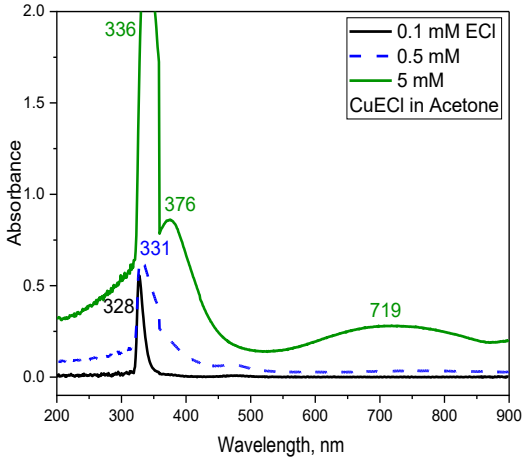

Figure 21. UV-Vis absorption spectra of ethyl 4-chloroacetoacetat (0.1 mM, black), CuECl (0.5 mM, blue and 5 mM, green) in Acetone

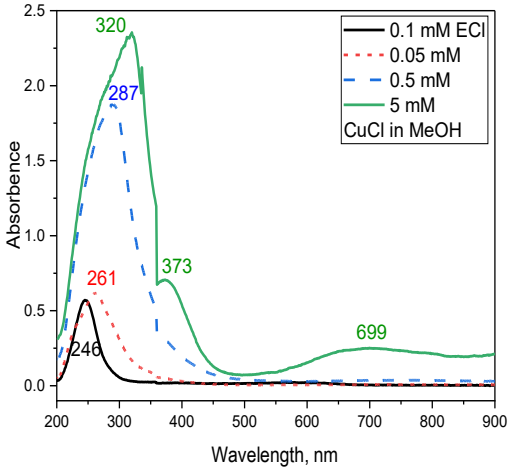

Figure 22. UV-Vis absorption spectra of ethyl 4-chloroacetoacetat (0.1 mM, black), CuECl (0.05 mM, red, 0.5 mM, blue and 5 mM, green) in MeOH

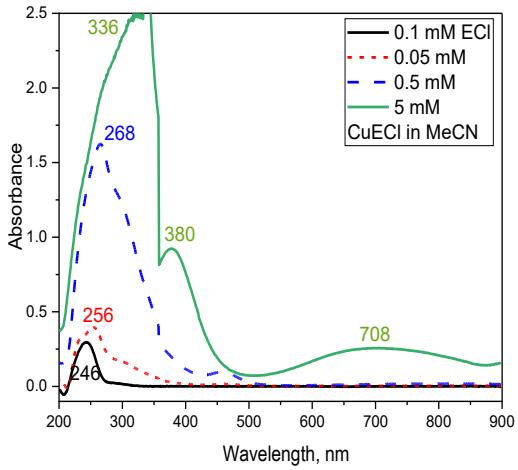

Figure 23. UV-Vis absorption spectra of ethyl 4-chloroacetoacetat (0.1 mM, black), CuECl (0.05 mM, red, 0.5 mM, blue and 5 mM, green) in MeCN

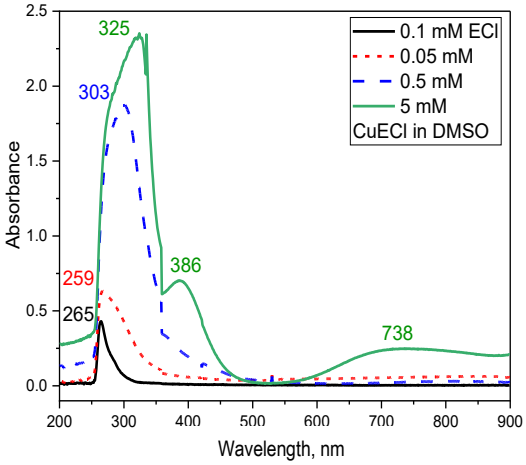

Figure 24. UV-Vis absorption spectra of ethyl 4-chloroacetoacetat (0.1 mM, black), CuECl (0.05 mM, red, 0.5 mM, blue and 5 mM, green) in DMSO

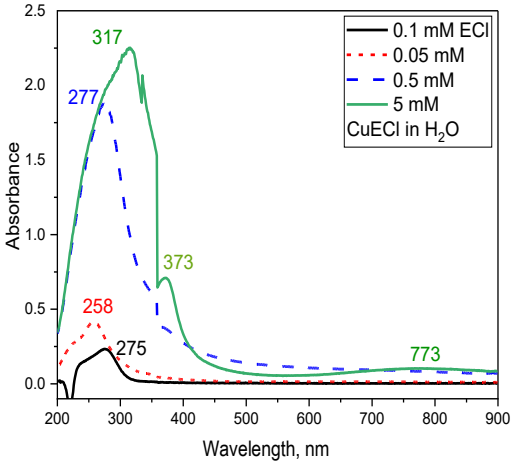

Figure 25. UV-Vis absorption spectra of ethyl 4-chloroacetoacetat (0.1 mM, black), CuECl (0.05 mM, red, 0.5 mM, blue and 5 mM, green) in H_2O

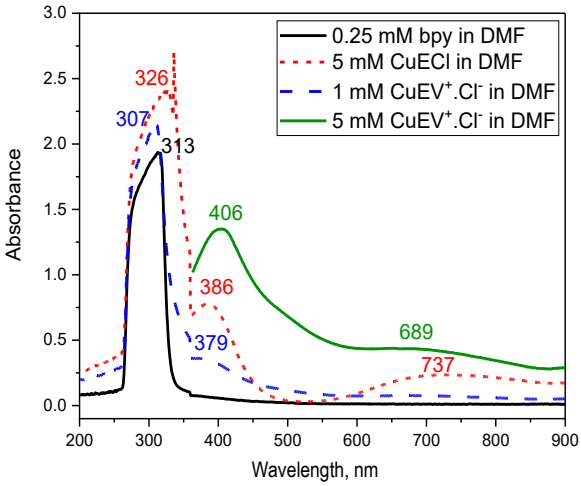

Figure 26. UV-Vis absorption spectra of bpy (0.25 mM, black), CuECl (5 mM, red), $CuEV^{+}.Cl^{-}$ (1 mM, blue and 5 mM, green) in DMF

The *d–d* electronic transition bands for CuECl and copper(II) acetate were detected at wavelengths of 697 nm and 700 nm in ethanol, and at 737 nm and 704 nm in DMF, respectively. Compared to copper(II) acetate, the CuECl bands exhibit hypsochromic shifts of 3 nm in ethanol and 33 nm in DMF, indicating the formation of a coordination complex between the Cu^{2+} center and the ECl ligand. Furthermore, the UV absorption band of CuECl in ethanol appears at 257 nm, which is blue-shifted relative to copper(II) acetate (300 nm), suggesting more energetic electronic transitions within the complex. The ligand ECl displays multiple absorption bands in the same solvents at 249, 328, 259, 246, 250, 246, 271, 265, and 275 nm, respectively, reflecting its inherent electronic transitions [31].

These UV absorptions of ECl is oscillatory with increasing of solvent polarity [31]. With respect to polarity, the non-bonding (*n*) orbital exhibits greater polarity than the π* orbital, which itself is more polar than the π orbital. In solvents of higher polarity, both the π and π* orbitals experience stabilization, albeit to differing degrees. Because the π* orbital is more polar than the π-orbital, so in a more polar solvent, the magnitude of stabilizing of π* orbital of the highest energy will be greater than the magnitude of stabilizing of π orbited of the at lower energy levels, the stabilization of the π* orbital in a more polar solvent is greater than that of the π orbital. Consequently, the energy gap (ΔE) between the π and π* orbitals decreases as solvent polarity increases [32]. As a result, the maximum absorption wavelength (λ_max) in a more polar solvent becomes larger than that in a less polar solvent (since $\Delta E \propto 1/\lambda\_max$). This leads to a bathochromic (red) shift of the π–π* absorption band in polar media [33].

It is valuable to examine the influence of solvent polarity on the λ_max of the n–π* transition. In highly polar solvents, both the non-bonding (*n*) and antibonding (π*) orbitals undergo stabilization, albeit to varying degrees. Due to the higher polarity of the *n* orbital relative to the π* orbital, its stabilization is more pronounced in polar media. Consequently, the energy of the *n* orbital decreases to a greater degree than that of the π* orbital. This results in an enlarged energy gap between the *n* and π* orbitals relative to that in less polar solvents. This results in a hypochromic (blue) shift of the *n*→π* transition, i.e., the λ_{max} of this transition decreases as solvent polarity increases. Conversely, the more intense π→π* transition exhibits a bathochromic (red) shift with increasing solvent polarity. Thus, as solvent polarity rises, the π-π* and *n*-π* transitions approach each other in wavelength. For the ECl ligand, intra-molecular hydrogen bonding within the solution further stabilizes resonance structures, lowering the energy of the π→π* transition. Simultaneously, hydrogen bonding weakens the *n*→π* transition, contributing to its blue shift. The combined effect of orbital polarity differences, solvent stabilization, Hydrogen bonding causes the *n*→π* and π→π* transitions to converge, effectively causing the high-intensity π→π* band to overlap with the lower-intensity *n*→π* band in the ECl ligand [31].

The UV absorptions of the weaker ligand ECl (249 nm, 328 nm, 259 nm, 246 mm, 250 nm, 246 nm, 271 nm, 265 nm and 275 nm) are red shifted [31]. This reflects the energetically easier transitions for the ligand ECl. These easier UV transition could be related to the longer extended conjugation system in the ligand ECl due to the existence of Cl atom. Except for ECl in H_2O, both the complex of CuECl showed red shifted UV transitions compared with those of the ligand of ECl respectively. The easier UV transition of the complexes could be related that upon complexation with Cu^{2+} ion, The established structure of the free ligand ECl adopts a more planar geometry upon coordination in the CuECl complex [34]. This increased planarity facilitates greater electron delocalization (resonance) within the complex, relative to the free ligand, leading to bathochromic (red) shifts in the UV absorption spectra of the complexes. In general, the shifts in wavelength positions and variations in absorption intensities of the UV bands observed for the copper complexes relative to their ligands provide clear evidence for the coordination of Copper(II) ions induces a greater planarity in the resulting complexes relative to the corresponding free ligands [35–38].

The visible absorption bands occur as a result of electronic transitions between split d-electron energy levels. In the visible region of the spectrum, of CuECl showed two bands, sharp band of higher energy and the second is broad with lower energy in different solvents attributed to the intra-atomic *d–d* transitions of the copper(II) ion in the complex [37].

This band can be assigned to the electronic transition *dxz*, *dyz* → *dxy* [32]. Two weak-defined bands appeared of CuECl as one broad band due to $dz^2 \rightarrow dxy$ transitions respectively. This broad band occurred at 687, 687, 719, 677, 708, 697, 656, 737, 738 and 773 nm in benzene, EtOAc, Acetone, MeCN, DCM, EtOH, MeOH, DMF, DMSO and H_2O respectively. In same solvents, (except H_2O). These three single electron *d-d* transitions are consonant with square planar CuECl complexe (Cu^{2+} with a d^9 configuration). The square planer Cu^{2+} d^9 configuration has four-fold splitting with decreasing energy in the following order: $dxz, dyz < dz^2 < d^2x^2 — y^2 < dxy$ [32–37].

The reaction of CuECl that have positive axial ligands (very weak ligands). These uncommon complexes are very sparingly soluble complexes showed very exceptional behavior in DMF media. The axial coordinated viologen within these complexes are reduced at dissolving only in DMF at air atmosphere [38, 39].

The S_N2 nucleophilic substitution of the complexes CuECl, with each of bpy, affords the complexe $CuEV^{+}\cdot Cl^{-}$. In these exceptional complexes, the complexed β-ketoester ligand has been modified to positive ligand within the complexes structures. The Ultraviolet-Vis absorption spectrum of these complexes are recorded in DMF media and presented in Figures 16–26. The purple color of $CuEV^{+}\cdot Cl^{-}$ solution in DMF refers undoubtedly to the generation of a π-dimeric association involving two $V^{\bullet}$ radicals within two complexes. Also, the peaks occurred at 406 nm and 689 nm are juxtapose to the formation of non-dimer viologen radical ($V^{\bullet}$) consequently there is an equilibrium among non-dimerized viologen radical $V^{\bullet}$ and dimerized viologen radicals stand $(C_1V)_2$ within $CuEV^{+}\cdot Cl^{-}$ structures [37–39] (Scheme 3).

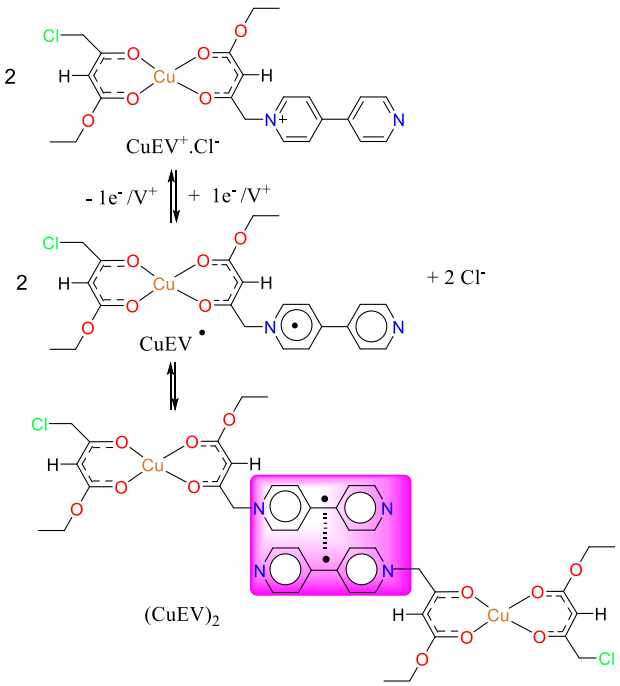

Scheme 3. Inter-molecular dimerized viologen radicals of $CuEV^{+}\cdot Cl^{-}$ in DMF

Formation of Molecular Switches: Reduction of Viologen Units within the Complexes

The UV-Visible absorption spectra were obtained after reducing the mixtures using solvation in Zn powder, with concentrations of 0.5 mM for $CuEV^{+}\cdot Cl^{-}$. In these cases the viologen formed complexes terminal linkage with CuECl. Additionally, reduction was carried out using activated zinc powder. The absorption spectra were recorded over a range of 190–900 nm and are presented in Figures 27 and 28.

The viologen-terminated copper(II) complex, $CuEV^{+}\cdot Cl^{-}$, was reduced using activated Zn powder and monitored via UV-Vis absorption spectroscopy. To accurately track the spectral changes associated with the reduction of the viologen units (both in the free ligand and when coordinated to the Cu(II) center), two reference blanks were employed: the pure DMF solvent and the non-reduced complex solution.

In Cu(II)-viologen complex of $CuEV^{+}\cdot Cl^{-}$, viologen radical cations are formed as a consequence of the reduction ($V^{\bullet+}$), which dimerize into $[V^{\bullet+}]_2$ dimers through strong π-π stacking interactions. The spectral shift from 550–600 nm to 700–800 nm, along with the distinct appearance of peaks near 800 nm in all compounds, indicates the successful reduction and the subsequent formation of dimers. This observed dimer formation is consistent with the mechanism proposed in Scheme 4. The presence of Cu(II) can modulate the stability and redox properties of the dimer, differentiating the behavior of coordinated vs. free viologen radicals [40–43].

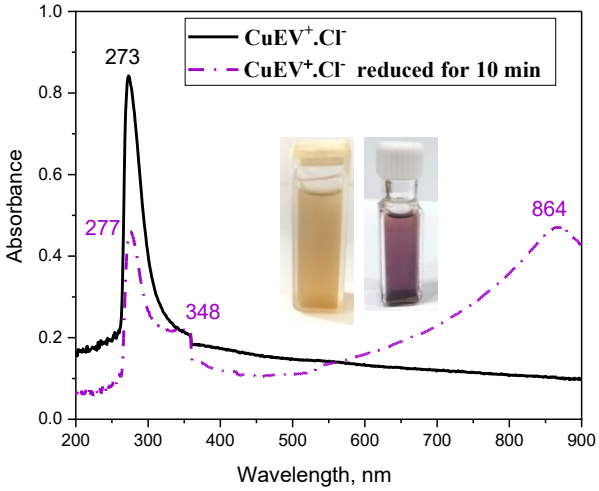

Figure 27. UV-Vis absorption spectra of $CuEV^{+}\cdot Cl^{-}$ (0.5 mM, Black) and reduced $CuEV^{+}\cdot Cl^{-}$ (0.5 mM, Purple) in DMF. Reference blank: $CuEV^{+}\cdot Cl^{-}$ (0.5 mM)

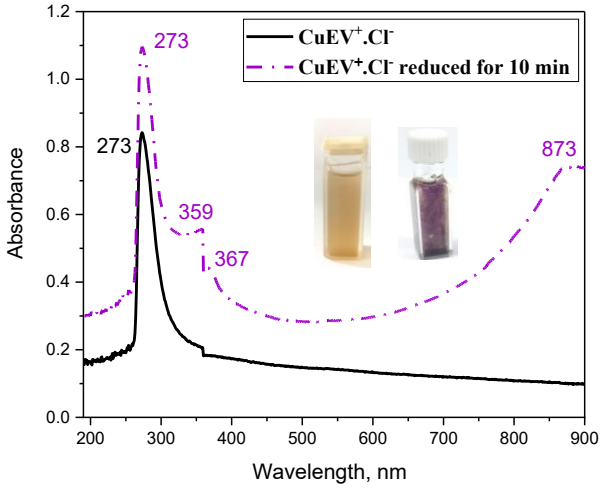

Figure 28. UV-Vis absorption spectrum of $CuEV^{+}\cdot Cl^{-}$ (0.5 mM, Black) and reduced $CuEV^{+}\cdot Cl^{-}$ (0.5 mM, Purple) in DMF. Reference blank: DMF

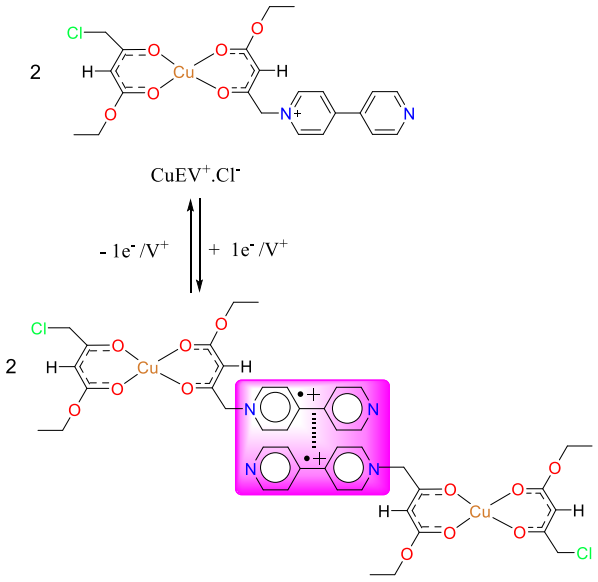

Scheme 4. Inter-molecular dimerized viologen radicals of $CuEV^{+}\cdot Cl^{-}$ in DMF

Electrochemical Studies of Molecular Switches

The electrochemical behavior of the ECl ligand, its corresponding copper(II) coordination complexes, bpy adducts, and the viologen-terminated species ($CuEV^{+}\cdot Cl^{-}$) was systematically examined in DMF containing 0.1 M TBAP as the supporting electrolyte by means of cyclic voltammetry (CV). All reported potentials are referenced to a silver pseudo-reference electrode. To minimize oxidative degradation of the electrogenerated species, all voltammetric measurements were performed at ambient laboratory temperature under an inert argon atmosphere. A conventional three-electrode setup was employed, consisting of a glassy carbon disk as the working electrode and a platinum wire as the counter electrode. Additional experimental conditions for each voltammogram are provided in the experimental section or indicated in the figure captions.

The cyclic voltammograms (CVs) of the complex CuECl are depicted in Figures 29 and 30 respectively. These CVs will be compared with the CVs of their precursor: $Cu(OAc)_2$ and ECl that are presented in Figures 31–33 respectively. An irreversible reduction process of the free ECl ligand was observed at –2.025 V respectively at f 0.3 V/s. The irreversible oxidation of Cu^{2+} ion in $Cu(OAc)_2$ is noted at 845.666 mv rt 0.3 V/s see Figure 32.

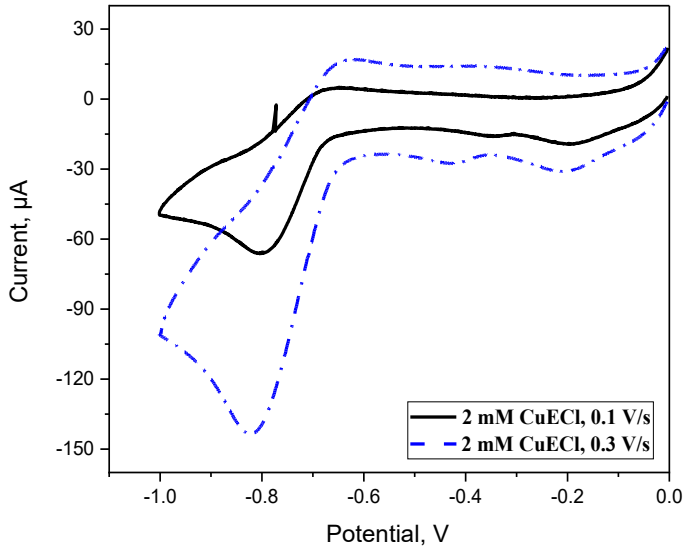

Figure 29. Cyclic voltammograms (CVs) of 2 mM CuECl in DMF (0.1M TBAP) at scan rates of 0.1 V/s (black) and 0.3 V/s (blue dashed). WE: (3 mm) VC. RE: Ag

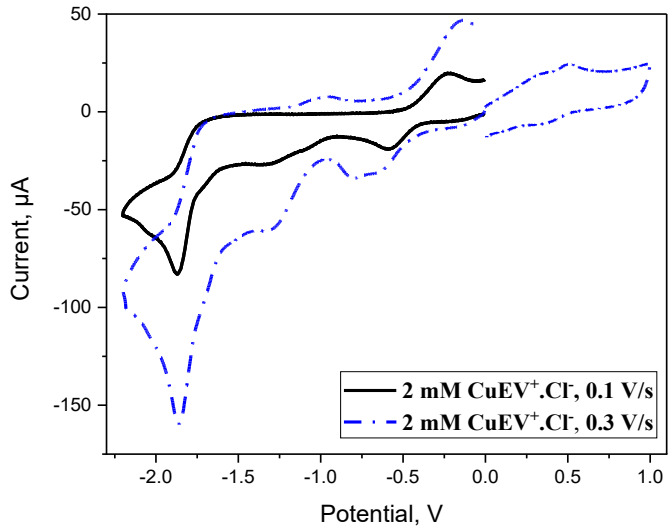

Figure 30. Cyclic voltammograms (CVs) of 2 mM $CuEV^{+}\cdot Cl^{-}$ in DMF (0.1M TBAP) at scan rates of 0.1 V/s (black) and 0.3 V/s (blue dashed). WE: (3 mm) VC. RE: Ag

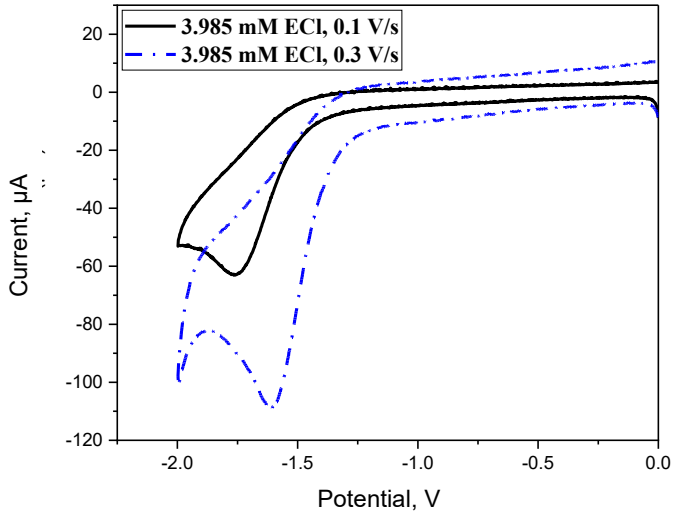

Figure 31. Cyclic voltammograms (CVs) of 3.985 mM ECl in DMF (0.1M TBAP) at scan rates of 0.1 V/s (black) and 0.3 V/s (blue dashed). WE: (3 mm) VC. RE: Ag

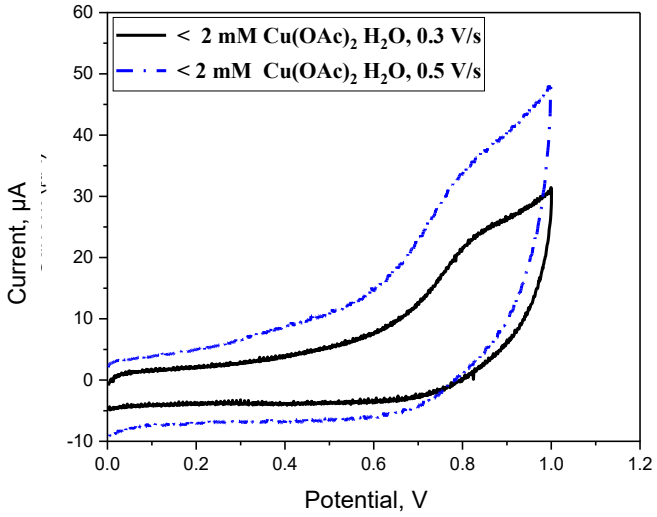

Figure 32. Cyclic voltammograms (CVs) of less than 2 mM $Cu(OAC)_2$ in DMF (0.1M TBAP) at scan rates of 0.1 V/s (black) and 0.3 V/s (blue dashed). WE: (3 mm) VC. RE: Ag

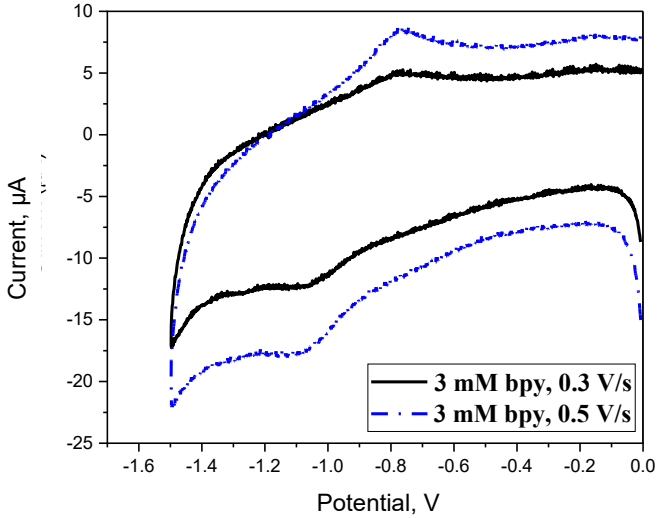

Figure 33. CVs of 3 mM bpy in DMF (0.1M TBAP) at scan rates of 0.3 V/s (black) and 0.5 V/s (blue dashed). WE: (3 mm) VC. RE: Ag

The reduction of Cu^{2+} ion in the complexe CuECl occured at –346.348 mv respectively. The of CuECl (–4571.19 mv) is consistent with the more electron deficiency of Cu^{2+} ion in the complex CuECl. The reduction of the coordinated ECl in the complex CuECl respectively is noted at –804.26 mv. Here, the coordinated ECl suffers more electron deficiency than the coordinated E which in turns lends to easier reduction for the coordinated ECl. Both the reduction of the coordinated ECl is anodically shifted compared with the reduction of the free ECl. These shift reflect the decrease of the electron densities of the ligands after complexations.

The nucleophilic substitution (S_N2) of the complex CuECl with each of bpy afford the complexe bearing the viologen units within their ligands: $CuEV^{+}\cdot Cl^{-}$. The CVs of these novel complexes are presented in Figures 3.176, 3.178 and 3.179 respectively. The reductions of viologen unit in $CuEV^{+}\cdot Cl^{-}$ are anodically shifted shifted to be at –646.536 mv and –813.768 mv. The observed shifts are clearly ascribed to the formation of intermolecular π-dimers between viologen radicals ($V^{\bullet}\ldots V^{\bullet}$) from two $CuEV^{+}\cdot Cl^{-}$ complexes. The reduction at –1326 mv could be assigned to the formation of ($V^{\bullet}$) followed by the formation of π-dimer with different conformation. The reduction of the coordinated ECl happened at –1878 mv easier than the free ECl ligand. The oxidation process happened at –918.278 mv could be related to the oxidation of the previous reduced species that have been absorbed on the electrode while, the reduction of the coordinated Cu^{2+} ion $Cu^{2+} + 1e^{-} \rightarrow Cu^{+}$ is not seen well, its oxidation process is not at –77.903 mv.

The reduction noted at –1528 mv is assigned to the coordinated ECl. The reduction of the coordinated Cu^{2+} ion to Cu^{+} is noted at –472.941 mv and the oxidation of the resulted Cu^{+} species happened at –269.134 mv [44–46].

Our electrochemical results, supported the formation of the complexes and showed well the electronic properties of the coordinated Cu(II) ion, ligands and viologen units.

Conclusions

In this study, two complementary design strategies were successfully established for the incorporation of viologen redox units into copper(II) β-diketone frameworks, enabling systematic modulation of structural and electrochemical properties. The first strategy involved axial coordination of the viologen moiety to preformed Cu(II) β-diketone complexes, whereas the second relied on the structural integration of the viologen (or bpy) unit within the β-diketone ligand prior to complexation. These approaches provide a controlled platform for tuning structure–property relationships in copper-based redox-active systems. The formation of CuECl and $CuEV^{+}\cdot Cl^{-}$ was confirmed by mass spectrometry, elemental analysis, and spectroscopic techniques, while XRD and SEM analyses revealed well-defined nanocrystalline domains whose morphology and crystallite size depend strongly on ligand functionalization. Crystallite sizes calculated using Scherrer and Williamson–Hall models, together with lattice strain analysis, demonstrated that viologen incorporation significantly influences microstructural parameters. Thermal studies further showed enhanced stability for CuECl relative to $CuEV^{+}\cdot Cl^{-}$, with all decomposition stages being endothermic and entropy-driven, reflecting the robustness of the coordination framework.

The electronic absorption spectra of the CuECl complex were recorded at three different concentrations (0.05 mM, 0.5 mM, and 5 mM) in various solvents to examine solvent effects on electronic transitions, electronic absorption studies confirmed the preservation of ligand-centered π–π* and *n*–π* transitions upon coordination, in addition to characteristic *d*–*d* bands consistent with square-planar Cu(II) geometry.

Notably, the intense violet coloration of $CuEV^{+}\cdot Cl^{-}$ in DMF and the absorption bands at 406 and 689 nm provide clear spectroscopic evidence for reversible equilibrium between monomeric viologen radicals and π-dimer species. Cyclic voltammetry further demonstrated that both coordination modes preserve the redox activity of the viologen unit, enabling controlled switching between radical and π-dimer states under chemical and electrochemical stimuli.

Overall, the present work establishes a versatile synthetic and structural framework for integrating viologen-based molecular switches into copper(II) β-diketone systems. The demonstrated correlation between coordination mode, crystallinity, thermal stability, and redox-switching behavior offers valuable design principles for the development of responsive inorganic–organic hybrid materials and copper-based molecular electronic platforms.

Supporting Information

The Supporting Information is available free at https://ejc.buketov.edu.kz/ejc/article/view/548/399

*Author Information**

**The authors' names are presented in the following order: First Name, Middle Name and Last Name*

Ahmed Abd alridha Alibrahimi (*corresponding author*) — Assistant Professor, Department of Chemistry, College of Science, University of Thi-Qar, 64001, Nassiria, Iraq; e-mail: ahmedoudah501@gmail.com; https://orcid.org/0000-0002-3271-9015

Wathiq Sattar Abdul-Hassan — Professor, Department of Chemistry, College of Science, University of Thi-Qar, 64001, Nassiria, Iraq; e-mail: Wathiq.a_chem@sci.utq.edu.iq; https://orcid.org/0000-0003-1297-3822

Author Contributions

The manuscript was written through contributions of all authors. All authors have given approval to the final version of the manuscript. CRediT: **Ahmed Abd alridha Alibrahimi** conceptualization, data curation, formal analysis, investigation, methodology, validation, visualization, writing-review & editing; **Wathiq Sattar Abdul-Hassan** conceptualization, data curation, formal analysis, funding acquisition, resources, supervision, validation, writing-original draft, writing-review & editing.

Acknowledgments

Both authors extend their thanks and appreciation to: *Department of Chemistry, College of Science, University of Thi-Qar*, and all those who helped us in this research.

Conflicts of Interest

The authors (*Ahmed Abd alridha Alibrahimi and Wathiq Sattar Abdul-Hassan*) declare no conflict of interest.

References

1 Lee, C.K., Gangadharappa, C., Fahrenbach, A.C., & Kim, D. J. (2024). Harnessing Radicals: Advances in Self-Assembly and Molecular Machinery. *Advanced Materials*, *36*(42), 2408271. https://doi.org/10.1002/adma.202408271

2 Zhang, D.W., Tian, J., Chen, L., Zhang, L., & Li, Z.T. (2015). Dimerization of Conjugated Radical Cations: An Emerging Non-Covalent Interaction for Self-Assembly. *Chemistry–An Asian Journal*, *10*(1), 56–68 https://doi.org/10.1002/asia.201402805

3 Carrington, M.E., Sokołowski, K., Jónsson, E., Zhao, E.W., Graf, A.M., Temprano, I., & Scherman, O.A. (2023). Associative pyridinium electrolytes for air-tolerant redox flow batteries. *Nature, 623*(7989), 949–95. https://doi.org/10.1038/s41586-023-06664-7

4 Liu, L., Yao, Y., Wang, Z., & Lu, Y.C. (2021). Viologen radical stabilization by molecular spectators for aqueous organic redox flow batteries. *Nano Energy*, *84*, 105897. https://doi.org/10.1016/j.nanoen.2021.105897

5 Zhou, C., Tian, J., Wang, J. L., Zhang, D. W., Zhao, X., Liu, Y., & Li, Z.T. (2014). A three-dimensional cross-linking supramolecular polymer stabilized by the cooperative dimerization of the viologen radical cation. *Polymer Chemistry*, *5*(2), 341–345. https://doi.org/10.1039/C3PY01006F

6 Dalvand, P., Nono, K.N., Shetty, D., Benyettou, F., Asfari, Z., Platas-Iglesias, C., & Elhabiri, M. (2021). Viologen–cucurbituril host/guest chemistry–redox control of dimerization versus inclusion. *RSC advances*, *11*(47), 29543–29554. https://doi.org/10.1039/D1RA05488K

7 Imabayashi, S.I., Kitamura, N., Tokuda, K., & Tazuke, S. (1987). Intramolecular Association of Viologen Dimer and Trimer Radical Cations. An Electrochemical and Spectroscopic Study. *Chemistry Letters*, *16*(5), 915–918. https://doi.org/10.1246/cl.1987.915

8 Malik, M., Świtlicka, A., Bieńko, A., Komarnicka, U.K., Bieńko, D.C., Kozieł, S., ... & Machura, B. (2022). Copper (II) complexes with 2-ethylpyridine and related hydroxyl pyridine derivatives: structural, spectroscopic, magnetic and anticancer in vitro studies. *RSC advances*, *12*(42), 27648–27665. https://doi.org/10.1039/D2RA05133H

9 Rostas, A.M., Badea, M., Ruta, L.L., Farcasanu, I.C., Maxim, C., Chifiriuc, M. C., & Olar, R. (2020). Copper (II) complexes with mixed heterocycle ligands as promising antibacterial and antitumor species. *Molecules*, *25*(17), 3777. https://doi.org/10.3390/molecules25173777

10 El-Sayed, D.S., Tawfik, E.M., Elhusseiny, A.F., & El-Dissouky, A. (2023). A perception into binary and ternary copper (II) complexes: synthesis, characterization, DFT modeling, antimicrobial activity, protein binding screen, and amino acid interaction. *BMC chemistry*, *17*(1), 55. https://doi.org/10.1186/s13065-023-00962-x

11 Sebastian, S., Sylvestre, S., Sundaraganesan, N., Karthikeyan, B., & Silvan, S. (2022). Conformational analysis, molecular structure, spectroscopic, NBO, reactivity descriptors, wavefunction and molecular docking investigations of 5,6-dimethoxy-1-indanone: A potential anti Alzheimer's agent. *Heliyon*, *8*(1). https://doi.org/10.1016/j.heliyon.2022.e08821

12 Holtzclaw, H.F., Lintvedt, R.L., Baumgarten, H.E., Parker, R.G., Bursey, M.M., & Rogerson, P.F. (1969). Mass spectra of metal chelates. I. Substituent effects on ionization potentials and fragmentation patterns of some 1-methyl-3-alkyl-1, 3-dione-copper (II) chelates. *Journal of the American Chemical Society*, *91*(14), 3774–3778. https://doi.org/10.1021/ja01042a014

13 Turgambaeva, A.E., Bykov, A.F., & Igumenov, I.K. (1995). Investigation of the thermal decomposition of bis(acetylacetonato)copper(II) vapour by a mass spectrometric method. *Thermochimica acta*, *256*(2), 443–456. https://doi.org/10.1016/0040-6031(95)91302-Y

14 Jinan, A. Azouz, & Wathiq, S. Abdul-Hassan. (2025). Synthesis, characterization, and redox-responsive novel molecular switching behavior of copper(II)–Viologen adduct complexes. *Applied Chemical Engineering*. https://doi.org/10.59429/ace.v8i3.5751

15 Neelakantan, P. (1964, June). Raman spectrum of ethyl chloroacetate. In *Proceedings of the Indian Academy of Sciences-Section A* (Vol. 59, No. 6, pp. 385–389). New Delhi: Springer India. https://doi.org/10.1007/BF03049210

16 Köse, D.A. (2007). Synthesis and characterization of bis(nicotinamide)-m-hydroxybenzoate complexes of Co (II), Ni (II), Cu (II), and Zn (II). *Russian Journal of Inorganic Chemistry*, *52*(9), 1384–1390. https://doi.org/10.1134/S0036023607090124

17 Holtzclaw, H.F., Lintvedt, R.L., Baumgarten, H.E., Parker, R.G., Bursey, M.M., & Rogerson, P.F. (1969). Mass spectra of metal chelates. I. Substituent effects on ionization potentials and fragmentation patterns of some 1-methyl-3-alkyl-1, 3-dione-copper (II) chelates. *Journal of the American Chemical Society*, *91*(14), 3774–3778. https://doi.org/10.1021/ja01042a014

18 Turgambaeva, A.E., Bykov, A.F., & Igumenov, I.K. (1995). Investigation of the thermal decomposition of bis(acetylacetonato)copper(II) vapour by a mass spectrometric method. *Thermochimica acta*, *256*(2), 443–456. https://doi.org/10.1016/0040-6031(95)91302-Y

19 Azhar H. Gatea, Wathiq S. Abdul-Hassan. (2023). Ligand Adducts of Bis(acetylacetonato) Copper(II), Bis(3-chloroacetylacetonato) Copper(II) with 4,4'-bipyridine, and Propylene Spacered Bis-viologen. *Journal of Medicinal and Chemical Sciences*, *6*(2), 280–303. http://doi:10.26655/JMCHEMSCI.2023.2.10

20 Waseda, Y., Matsubara, E., & Shinoda, K. (2011). *X-ray diffraction crystallography: introduction, examples and solved problems*. Springer Science & Business Media. http://doi:10.1007/978-3-642-166355-8

21 Prabhu, Y.T., Rao, K.V., Kumar, V.S.S., & Kumari, B.S. (2014). X-ray analysis by Williamson-Hall and size-strain plot methods of ZnO nanoparticles with fuel variation. *World Journal of Nano Science and Engineering*, *2014*. http://dx.doi.org/10.4236/wjnse.2014.41004

22 Lalancette, R.A., Syzdek, D., Grebowicz, J., Arslan, E., & Bernal, I. (2019). The thermal decomposition and analyses of metal tris-acetylacetonates: Free radical formation from Al, Cr, Mn, Fe and Co complexes. *Journal of Thermal Analysis and Calorimetry*, *135*(6), 3463–3470. https://doi.org/10.1007/s10973-018-7598-8

23 Sheikh, J., Juneja, H., Ingle, V., Ali, P., & Hadda, T.B. (2013). Synthesis and in vitro biology of Co (II), Ni (II), Cu (II) and Zinc (II) complexes of functionalized beta-diketone bearing energy buried potential antibacterial and antiviral O,O pharmacophore sites. *Journal of Saudi Chemical Society*, *17*(3), 269–276. https://doi.org/10.1016/j.jscs.2011.04.004

24 Jassema, I.A., Abdul-Hassana, W.S., Flafela, I.A., & Jghebilb, H.O. (2023). Axial ligation for copper (II) complexes of bis(acetylacetonato)ethylenediimine and bis(3-chloroacetylacetonato)ethylenediimine. *Journal of Medicinal and Pharmaceutical Chemical Research*, 5, 173–203 https://doi.org/10.22034/ecc.2023.363684.1533

25 Lalancette, R.A., Syzdek, D., Grebowicz, J., Arslan, E., & Bernal, I. (2019). The thermal decomposition and analyses of metal tris-acetylacetonates: Free radical formation from Al, Cr, Mn, Fe and Co complexes. *Journal of Thermal Analysis and Calorimetry*, *135*(6), 3463–3470. https://doi.org/10.1007/s10973-018-7598-8

26 Chrissafis, K., Lalia-Kantouri, M., & Aslanidis, P. (2011). Kinetic analysis of the thermal decomposition of copper (I) complexes with heterocyclic thiones. *Journal of thermal analysis and calorimetry*, *104*(3), 1045–1050. https://doi.org/10.1007/s10973-010-1164-3

27 Farrukh, M. A., Butt, K.M., Chong, K.K., & Chang, W.S. (2019). Photoluminescence emission behavior on the reduced band gap of Fe doping in CeO_2-SiO_2 nanocomposite and photophysical properties. *Journal of Saudi Chemical Society*, *23*(5), 561–575. https://doi.org/10.1016/j.jscs.2018.10.002

28 Vigato, P.A., Peruzzo, V., & Tamburini, S. (2009). The evolution of β-diketone or β-diketophenol ligands and related complexes. *Coordination Chemistry Reviews*, *253*(7-8), 1099–1201. https://doi.org/10.1016/j.ccr.2008.07.013

29 Papatriantafyllopoulou, C., Efthymiou, C.G., Raptopoulou, C.P., Vicente, R., Manessi-Zoupa, E., Psycharis, V., ... & Perlepes, S.P. (2007). Initial use of the di-2-pyridyl ketone/sulfate "blend" in 3d-metal cluster chemistry: Preparation, X-ray structures and physical studies of zinc (II) and nickel (II) cubanes. *Journal of molecular structure*, *829*(1–3), 176–188. https://doi.org/10.1016/j.molstruc.2006.06.022

30 Lindoy, L.F., Moody, W.E., & Taylor, D. (1977). Mass spectral and nuclear magnetic resonance (proton and carbon-13) study of metal complexes of quadridentate ligands derived from 1, 2-diaminoethane and substituted. beta-diketones; x-ray structure of N,N'-ethylenebis(5,5-dimethyl-4-oxohexan-2-iminato)nickel (II). *Inorganic Chemistry*, *16*(8), 1962–1968. https://doi.org/10.1021/ic50174a027

31 Martell, A.E., Belford, R.L., & Calvin, M. (1958). Influence of fluorine substitution on the properties of metal chelate compounds—II copper (II) chelates of tetradentate ligands. *Journal of Inorganic and Nuclear Chemistry*, *5*(3), 170–181. https://doi.org/10.1016/0022-1902(58)80127-X

32 Raman, N., Ravichandran, S., & Thangaraja, C. (2004). Copper (II), cobalt (II), nickel (II) and zinc (II) complexes of Schiff base derived from benzil-2,4-dinitrophenylhydrazone with aniline. *Journal of Chemical Sciences*, *116*(4), 215–219. https://doi.org/10.1007/BF02708270

33 Bünzli, J.C.G., & Piguet, C. (2005). Taking advantage of luminescent lanthanide ions. *Chemical Society Reviews*, *34*(12), 1048–1077. https://doi.org/10.1039/B406082M

34 Hassan, W.M., Zayed, E.M., Elkholy, A.K., Moustafa, H., & Mohamed, G.G. (2013). Spectroscopic and density functional theory investigation of novel Schiff base complexes. *Spectrochimica Acta Part A: Molecular and Biomolecular Spectroscopy*, *103*, 378–387. https://doi.org/10.1016/j.saa.2012.10.058

35 Vishwakarma, P.K., Mir, J.M., & Maurya, R.C. (2016). Pyrone-based Cu (II) complexes, their characterization, DFT based conformational drift from square planar to square pyramidal geometry and biological activities. *Journal of Chemical Sciences*, *128*(4), 511–522. https://doi.org/10.1007/s12039-016-1048-6

36 Faisal, A., & Maktoof, A. (2025). Analysis of Physical Properties and Evaluation of Heavy Element Concentrations in Euphrates River's Fish in Nasiriyah City. *University of Thi-Qar Journal of Science*, *12*(1), 233–237. https://doi.org/10.32792/utq/utjsci/v12i1.1380

37 Al-khafaji, N., Al-khafaji, B.Y., & Al-Omar, D.K. (2024). Assessment the Effects of Heavy Elements on Some Hematological Parameter in CKD Patients Undergoing Hemodialysis in Thi-Qar Province/Iraq. *University of Thi-Qar Journal of Science*, *11*(2), 54-58. https://doi.org/10.32792/utq/utjsci/v11i2.1192

38 Ding, C.C., Wu, S.Y., Xu, Y.Q., Wu, L.N., & Zhang, LJ. (2018). DFT studies for three Cu (II) coordination polymers: geometrical and electronic structures, g factors and UV–visible spectra. *Chemical Physics*, *508*, 20–25. https://doi.org/10.1016/j.chemphys.2018.04.016

39 Bamigboye, M., Mustapha, A., & Danjuma, F. (2024). Bioactivity Assessment of 8-Hydroxyquinoline and Monosodium Glutamate Mixed Ligand Copper Complex: Experimental and Computational. *University of Thi-Qar Journal of Science*, *11*(2), 175–184. https://doi.org/10.32792/utq/utjsci/v11i2.1302

40 Wasielewski, M.R. (1992). Photoinduced electron transfer in supramolecular systems for artificial photosynthesis. *Chemical reviews*, *92*(3), 435–461. https://doi.org/10.1021/cr00011a005

41 Abruña, H.D., Denisevich, P., Umana, M., Meyer, T.J., & Murray, R.W. (1981). Rectifying interfaces using two-layer films of electrochemically polymerized vinylpyridine and vinylbipyridine complexes of ruthenium and iron on electrodes. *Journal of the American Chemical Society*, *103*(1), 1–5. https://doi.org/10.1021/ja00391a001

42 Markel, F., Ferris, N.S., Gould, I.R., & Myers, A.B. (1992). Mode-specific vibrational reorganization energies accompanying photoinduced electron transfer in the hexamethylbenzene/tetracyanoethylene charge-transfer complex. *Journal of the American Chemical Society*, *114*(15), 6208–6219. https://doi.org/10.1021/ja00041a045

43 Chambron, J.C., Harriman, A., Heitz, V., & Sauvage, J.P. (1993). Ultrafast photoinduced electron transfer between porphyrinic subunits within a bis (porphyrin)-stoppered rotaxane. *Journal of the American Chemical Society*, *115*(14), 6109–6114. https://doi.org/10.1021/ja00067a028

44 Koomson, D.A., Nicholson, J.H., Brogan, A.P., & Aldous, L. (2024). Re-assessing viologens for modern bio-electrocatalysis. *Chemical Science*, *15*(24), 9325–9332. https://doi.org/10.1039/D4SC02431A

45 Nucera, A., Rizzuto, C., Pipita, M. M., Barba Castagnaro, I., Termine, R., Barberi, R. C., & Castriota, M. (2024). The Effects of Polymerization on the Performance of Viologen-Based Electrochromic Devices. *Gels*, *10*(11), 694. https://doi.org/10.3390/gels10110694

46 Monk, P.M., Turner, C., & Akhtar, S.P. (1999). Electrochemical behaviour of methyl viologen in a matrix of paper. *Electrochimica acta*, *44*(26), 4817–4826. https://doi.org/10.1016/S0013-4686(99)00225-X